2016년 2월

석사학위 논문

Development of high-performance epoxy nanocomposite using functionalized graphene oxide

조 선 대 학 교 대 학 원

탄소소재학과

유 진 원

Development of high-performance epoxy nanocomposite using functionalized graphene oxide

기능화 산화 그래핀을 이용한 고성능 에폭시 복합체의 개발

2016년 2월 25일

조 선 대 학 교 대 학 원

탄소소재학과

유 진 원

기능화 산화 그래핀을 이용한 고성능 에폭시 복합체의 개발

지도교수 이 재 관

이 논문을 이학석사학위신청 논문으로 제출함.

2015 11월

조 선 대 학 교 대 학 원

탄소소재학과

유 진 원

유진원의 석사학위논문을 인준함

위원장 조선대학교 교수 손 홍 래 (인)

위 원 조선대학교 교수 이 재 관 (인)

위 원 KIST 선임연구원 고 문 주 (인)

2015년 11월

조 선 대 학 교 대 학 원

Table of contents

List of figures

Figure 2.6 Glass transition temperatures (T_g) of EP/DDS/diamine-GO nanocomposites. T_g was estimated from the second heating DSC results of EP/DDS/diamine-GO mixture.

Figure 2.7 DMA results of EP/DDS/DDS-GO nanocomposites. (a) Storage modulus, (b) tanδ, and (c) crosslink density of the EP/DDS/DDS-GO nanocomposites. Samples were tested in a temperature range of 30 to 260 ℃ at a scanning rate of 3 ℃ /min. The crosslink density was calculated using storage modulus and tanδ in the rubbery region of EP/DDS/diamine-GO nanocomposites.

Figure 28 Tensile strengths of EP/DDS/diamine-GO nanocomposites. It was estimated by using a universal testing machine. Samples for measurement were prepared with 1.5 mm × 50 mm × 250 mm size, and tests were performed with a testing speed of 5 mm/min.

List of table and scheme

Abstract

Development of high-performance epoxy nanocomposite using functionalized graphene oxide

Yu Jin Won
Advisor : Prof. Lee Jae-Kwan
Department of Carbon Materials
Graduate School of Chosun University

에폭시 나노 복합소재는 열적 및 기계적 특성이 뛰어나기 때문에 많은 분야에서 이용되고 있다. 그럼에도 불구하고, 많은 기업들은 더욱 우수한 열적 및 기계적 특성을 가지는 복합소재를 요구하고 있다. 그러므로 이 연구에서는 산화 그래핀 (GO)를 다이아민계 경화제를 공유 결합을 통해 기능화하여 부경화제를 제조하였고, 이것을 이용하여 열적 및 기계적 강도가 우수한 에폭시 나노복합소재를 제조하였다. 그 결과, 부경화제를 사용하여 제조되어진 에폭시 나노복합소재의 가교밀도는 240% 증가하였다. 또한, 가교 밀도가 증가함에 따라 제조된 에폭시 나노복합소재의 유리전이온도 (T_g)는 114%, 인장 강도 (MPa)는 120% 증가하였다. 본 연구를 통해 제조된 에폭시 나노복합소재는 자동차, 선박, 우주 항공 등 다양한 산업에서 응용될 것으로 기대된다.

Chapter 1.

General Introduction

1.1. Nanocarbon materials

1.1.1 Carbon fibers (CFs)

Carbon fibers (CFs) consist of fibers about 5~10 micrometres in diameter and composed mostly of carbon atoms. CFs are manufactured from organic polymer fiber such as polyacrylonitrile (PAN) [2], rayon[3,4] and pitch by carbonization at 1000 ~ 3000 ℃ [5]. CFs which are a new breed of high-strength materials, are mainly used as reinforcements in composite materials such as carbon fiber reinforced plastics, carbon-carbon composite, carbon fiber reinforced materials, and CFs reinforced cement. CFs offer the highest specific modulus and highest specific strength of all reinforcing fibers[1]. To produce carbon fiber, the carbon atoms are bonded together in crystals that are more or less aligned parallel to the long axis of the fiber as the crystal alignment gives the fiber high strength-to-volume ratio. Several thousand carbon fibers are bundled together to form a tow, which may be used by itself or woven into a fabric.

Figure 1.1. Picture of carbon fibers (CFs).

1.1.2 Carbon nanotubes (CNTs)

Carbon nanotubes (CNTs) are cylinder-type carbon nanomaterials of one or more layers of graphene [6]. CNTs consist of sp^2 bond like graphite, and are categorized by the number of carbon wall; single-walled (SWCNTs), double-walled (DWCNTs) and multi-walled (MWCNTs) [7, 8]. Diameters of SWCNTs and MCWNTs are commonly 0.8 to 2 nm and 5 to 20 nm, respectively. CNT lengths are constructed length-to-diameter ratio of up to 13,000,000 [6]. CNTs is used in several application such as nanotechnology, electrical engineering, optical science and materials science due to unique characterization. Especially, CNTs are appiled as fillers of various composite materials because of their outstanding thermal [9], mechanical [11], and electrical [10] properties.

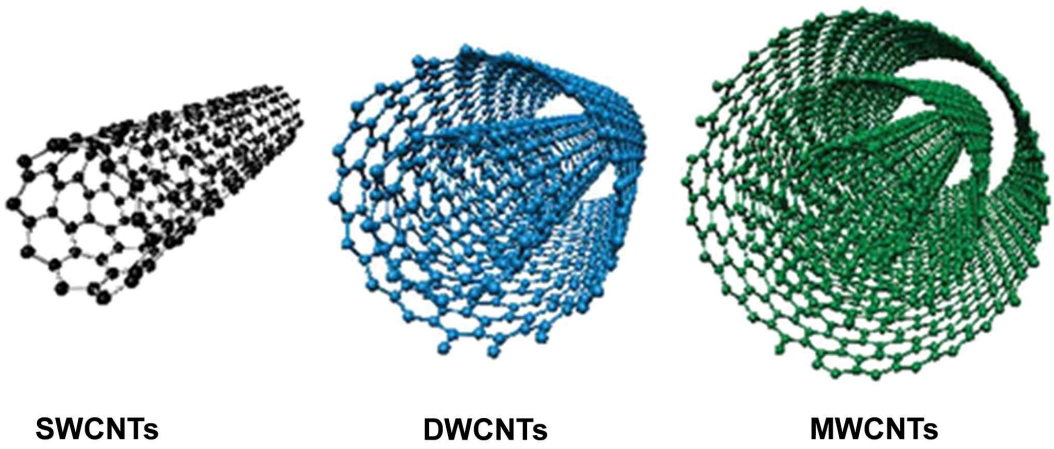

Figure 1.2. Structure of carbon nanotubr (CNTs).

1.1.3. Graphene and Graphene oxide

Graphene, a mono layer of sp^2 bonded carbon atoms, is a two dimensional (2D) material. Graphene has been attracting great interest because of its distinctive band structure and physical properties [12,13]. It is a unique material due to its extraordinary properties that include high electrical and thermal conductivity, high charge carrier density, carrier mobility, optical properties, trhermal stability, and mechanical properties. However, application of graphene to composite has been limited because of its low dispersion in organic solvent despite its high properties.

Graphene has been made by chemical vapor deposition (CVD) [17], the micromechanical exfoliation of graphite, Novoselove et al [18].

In order to improve the dispersion of graphene, graphene oxide (GO), which is produced by chemicals exfoliation of graphite, has been recently investigated as a novel carbon nanomaterial. On the surface of GO, some sp^2 carbons are converted into sp^3 carbons, and become bonded to oxygen moieties such as hydroxyl group and carboxylic acid group. Graphene oxide contains a range of reactive oxygen functional groups, which renders it a good candidate for use in the aforementioned applications through chemical functionalizations. GO is advantage cheap and mass production than graphene.

GO has been made by three different methods. The first is Brodie[14], Brodie was exploring the structure of graphite by investigating the reactivity of flake graphite. One of the reactions he performed involved adding potassium chlorate ($KClO_3$) to a slurry of graphite in fuming nitric acid (HNO_3). Brodie determined that the resulting material was composed of carbon, hydrogen, and oxygen, resulting in an increase.

The second is the sraudenmeier [15], This method is improved Brodie's $KClO_3$-fuming HNO_3 preparation by adding the chlorate in multiple aliquots over the course of the reaction (also, with the addition of concentrated sulfuric acid, to increase the acidity of the mixture), rather than in a single addition as Brodie

had done. This slight change in the procedure resulted in an overall extent of oxidation similar to Brodie's multiple oxidation approach, but performed more practically in a single reaction vessel. The third method is Hummers [16]. Hummers Developed an alternate oxidation method by reacting graphite with a mixture of potassium permanganate ($KMnO_4$) and concentrated sulfuric acid (H_2SO_4), again, achieving similar levels of oxidation.

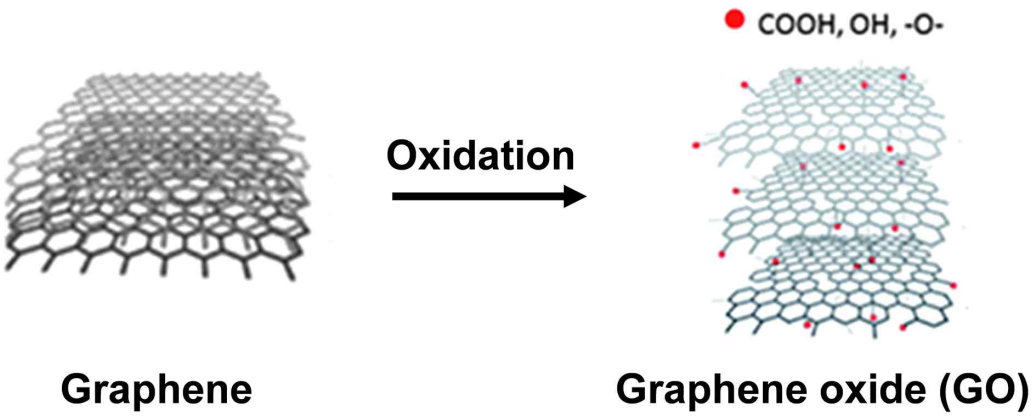

Figure 1.3. Structures of graphene and graphene oxide (GO).

1.2. Porous materials

Porous materials are of scientific and technological interest because of their ability to interact with atoms, ions and molecules not only at their surfaces, but throughout the bulk of the material. Not surprisingly, traditional applications of porous materials thus involve ion exchange, adsorption (for separation) and catalysis, and many of these benefit from the high order that can be achieved in solids such as zeolites. The pores of materilas are classified according to size: pore sizes in the range of 2 nm and below are called micropores, those in the range of 2 nm to 50 nm are denoted mesopores, and those above 50 nm are macropores. The distribution of sizes, shapes and volumes of the void spaces in porous materials directly relates to their ability to perform the desired function in a particular application. The need to create uniformity within the pore size, shape and volume has steadily increased over recent years because it can lead to superior applications properties [19]. For example, a material with uniform micropores, such as a zeolite, can separate molecules on the basis of their size by selectively adsorbing a small molecule from a mixture containing molecules too large to enter its pores [20]. Clearly, a distribution of pore sizes would limit the ability of the solid to separate molecules of differing sizes. A brief review on zeolites and molecular sieve syntheses that discusses these issues is available [20], as are reviews on microporous and ordered mesoporous materials syntheses and their applications as catalysts [21]. These materials provide the precedent for the ability to synthesize extra-large pore crystalline solids and apply them to a greater variety of commercially relevant applications.

1.3. Epoxy

Epoxy resin (EP), the most common thermosetting resin, forms a three-dimensional cross-linked network structure when subjected to exothermic curing. Epoxy resins are low molecular weight pre-polymers or higher molecular weight polymers which normally contain at least two epoxide groups. The epoxide group is also sometimes referred to as a glycidyl or oxirane group. Epoxy resin has been used in various industrial applications because of its good adhesion, chemical resistance, thermal resistance, and mechanical properties. However, despite its good properties, there has been a persistent demand for more functional EP that can be used in potential applications such as in automotive, aerospace, construction, and electronic industries. For example, various structure-modified EPs such as Bisphenol A type [22, 23], Bisphenol F type [24], novolac [25], cycloaliphatic [26], crystalline [27], and rubber-modified EPs [28] have been developed. Another attempt to improve the properties of cured EP has been to change curing agents and/or co-curing agents, which dramatically affect the thermal and mechanical properties of cured EP.

Bisphenol A is the most common and important class of epoxy resins. Bisphenol A is formed from reacting epichlorhydrin with bisphenol A to form diglycidyl ethers of bisphenol A. The simplest resin of this class is formed from reacting two moles of epichlorhydrin with one mole of bisphenol A to form the bisphenol A diglycidyl ether (commonly abbreviated to DGEBA or BADGE). DGEBA resins are transparent colourless-to-pale-yellow liquids at room temperature, with viscosity typically in the range of 5-15 Pa.s at 25°C. Industrial grades normally contain some distribution of molecular weight, since pure DGEBA shows a strong tendency to form a crystalline solid upon storage at ambient temperature.

Increasing the ratio of bisphenol A to epichlorhydrin during manufacture produces higher molecular weight linear polyethers with glycidyl end groups, which are semi-solid to hard crystalline materials at room temperature depending

on the molecular weight achieved. As the molecular weight of the resin increases, the epoxide content reduces and the material behaves more and more like a thermoplastic. Very high molecular weight polycondensates (ca. 30 000 – 70 000 g/mol) form a class known as phenoxy resins and contain virtually no epoxide groups (since the terminal epoxy groups are insignificant compared to the total size of the molecule). These resins do however contain hydroxyl groups throughout the backbone, which may also undergo other cross-linking reactions, e.g. with aminoplasts, phenoplasts and isocyanates [22, 23].

Bisphenol F may also undergo epoxidation in a similar fashion to bisphenol A. Compared to DGEBA, bisphenol F epoxy resins have lower viscosity and a higher mean epoxy content per gramme, which (once cured) gives them increased chemical resistance. Additionally, there is a higher proportion of trifunctional epoxy molecules, which increases the functionality available for crosslinking from 1.9 to 2.1 [24].

Novolac is that reaction of phenols with formaldehyde and subsequent glycidylation with epichlorhydrin produces epoxidised novolacs, such as epoxy phenol novolacs (EPN) and epoxy cresol novolacs (ECN). These are highly viscous to solid resins with typical mean epoxide functionality of around 2 to 6. The high epoxide functionality of these resins forms a highly crosslinked polymer network displaying high temperature and chemical resistance, but low flexibility [25].

Cycloaliphatic epoxy resin (CAE), 3′,4′-epoxycyclohexyl- methyl 3,4-epoxycyclohexanecarboxylate is synthesized by reacting 30-cyclohexenylmethyl 3-cyclohexenecarboxylate with peracetic acid. This epoxy resin has an aliphatic backbone and a fully saturated molecular structure, which contribute to its excellent UV stability, good weatherability, good thermal stability, and excellent electrical properties. These properties are crucial for resins used to fabricate structural components requiring application in hightemperature environments [26].

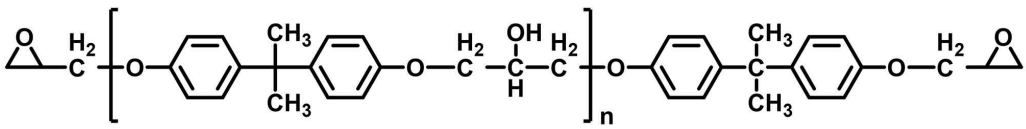

Bisphenol A type

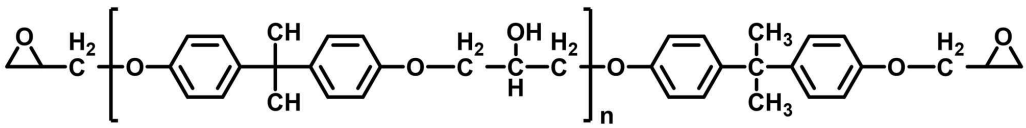

Bisphenol F type

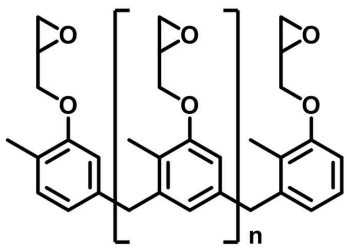

Novolac

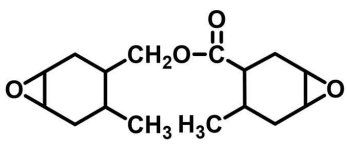

Cycloaliphatic

Figure 1.4. Structures of epoxy resins.

1.4. Reference

[1] W. S . Smyth, Engineered Materials Handbook-Vol. 1 49p, ASM International, USA, **(1987).**

[2] E. Fitzer, *ibid*. 27 621 **(1989).**

[3] R. Bacon, M. M. Tang, *Carbon* 2, 211 **(1964).**

[4] *Idem*. *ibid*. 2, 220 **(1964).**

[5] J. B. Donnet, R. C. Bansal, Carbon Fibers, Marcel Dekker, Inc., New York, **(1990)**.

[6] X. Wang, Q. Li, J. Xie, Z. Jin, J. Wang, Y. Li, K. Jiang, S. Fan, *Nano Lett.* 9, 3137 **(2009)**.

[7] S. Iijima, Nature 354, 56 **(1991)**.

[8] P. J. F. Harris, Carbon Nanotube Science - Synthesis, Properties, and Applications, Cambridge Univ. Press, Cambridge **(2009)**.

[9] E. Pop, D. Mann, Q. Wang, K. Goodson, H. J. Dai, *Nano Lett.* 6, 96 **(2006)**.

[10] W. Bauhofer, J. Z. Kovacs, *Compos. Sci. Technol.* 69, 1486 **(2009).**

[11] T.-W. Chou, L. Gao, E. T. Thostenson, Z. Zhang, J.-H. Byun, *Compos. Sci. Technol.* 70, 1 **(2010)**.

[12] C. N. R. Rao, A. K. sood, K. S. Subrahmanyam, A. Govindaraj, *Angew. chem. Int. Ed.* 48, 7752 **(2009)**.

[13] A. K. Geim, L. S. Novoselov, *Nat. Mater.* 6, 183 **(2007)**.

[13] B. C. Brodie, *Philos. Trans. R. Soc.* 149, 249 **(1859)**.

[14] L. Staudenmaier, *Ber. Dtsch. Chem. Ges.* 31, 1481 **(1898)**.

[15] W. S. Hummers, R. E. Offeman, *J. Am. Chem. Soc.* 80, 1339 **(1958)**.

[16] Y. P. Chen, Q. K. Yu, *nature nanotech.* 5, 559 **(2010)**.

[17] K. S. Novoselov, A. K. Geim, S. V. Morozov, D. Jiang, M. I. Katsnelson, I. V. Grigorieva, S. V. Dubonos, A. A. Firsov, *Nature* 438, 197 **(2005)**.

[18] M. B. Davis, *Nature* 417. 813 **(2002).**

[19] M. E. Davis, R. F. Lobo, *Chem. Mater.* 4, 756 **(1992).**

[20] A. Corma, *Chem. Rev.* 97, 2373 **(1997)**.

[21] A. M. Atta, N, O. Shaker, N. E. Nasser, *J. Appl. Polym. Sci.* 107, 347 **(2008).**

[22] K. Pivnenko, G. A. Pedersen, E. Eriksson, T. F. Astrup, *Waste Management* 44, 39 **(2015)**

[23] V. Dixit, A. K. Nagpal, R. Singhal, *Int. J. Plast. Technol.* 14, 38 **(2010)**

[24] J. R. Roxhester, A. L. Bolden, *Environ. Health. Persp.* 123, 643 **(2015)**

[25] P. Mohan, Polym. -Plast. technol. 52, 107 **(2013)**

[26] M. J. Yoo, S. H. Kim, S. D. Park, W.S. Lee, J.W. Sun, J.H. Choi, S. Nahm, Eur. Polym. J. 46, 1158 **(2010)**

[27] T. Song, Z. Li,; J. Liu, S. Yang, *Polym. Sci. Ser. B*, *55*, 147 **(2013)**

[28] B. J. P. Jansen, K. Y. Tamminga, H. E. H. Meijer, P. J. Lemstra, *Polymer*, 40, 5601 **(1999)**.

Chapter 2.

Enhancement of crosslink density, glass transition temperature, and strength of epoxy resin by using functionalized graphene oxide co-curing agents

2.1 Introduction

Epoxy resin (EP), the most common thermosetting resin, forms a three-dimensional cross-linked network structure when subjected to exothermic curing. Epoxy resin has been used in various industrial applications because of its good adhesion, chemical resistance, thermal resistance, and mechanical properties. However, despite its good properties, there has been a persistent demand for more functional EP that can be used in potential applications such as in automotive, aerospace, construction, and electronic industries. For example, various structure-modified EPs such as novolac [1], phenoxy [2], crystalline [3], and rubber-modified EPs [4] have been developed. Another attempt to improve the properties of cured EP has been to change curing agents and/or co-curing agents, which dramatically affect the thermal and mechanical properties of cured EP.

The use of carbon nanomaterials like carbon black [5], carbon nanotube [6–7], carbon nanofiber [8], and graphene [9–12] as fillers to prepare EP nanocomposites has been attracting attention owing to their unique properties. In addition to these nanomaterials, graphene oxide (GO) has been considered a promising nanomaterial for the improvement of the mechanical and thermal properties of polymer nanocomposites such as poly(methyl methacrylate), polystyrene, polyurethane, and poly(vinylidene fluoride) nanocomposites [13–14]. Various neat and functionalized GOs have also been adapted for enhancing the glass transition temperature (T_g) and/or mechanical strength of EP nanocomposites [15–20]. The crosslink density (CD) is generally recognized as a critical factor influencing the thermal [21–22] and mechanical [23–24] properties of EP nanocomposites. If the interfacial strength between the GO and EP is low, the CD of nanocomposites will be low, and because of the low CD value, improvements in the thermal and mechanical properties of EP nanocomposites can be not sufficient and, in some cases, these properties can worsen. In order to improve the interfacial strength between GO and EP, some studies focused

on the preparation of functionalized GOs with epoxide terminal groups [15–17] and with amine terminal groups [18–20]. In these studies, slight improvements in the T_g and tensile strength of cured EP nanocomposites compared to those of neat cured EPs were realized. Further, it has been mentioned that incorporation of nanomaterials into EP could slightly increase the CD of EP nanocomposites [25–30], but there have been few studies that calculated the CD of EP nanocomposites, made an effort to increase the CD of EP nanocomposite, and discussed an effect of the nanomaterials on the CD of EP nanocomposite.

In this work, I report a novel technique to improve the CD of GO-incorporated EP nanocomposites. I synthesized two diamine-functionalized GO, DDS-GO and HMDA-GO, by introducing 4,4′-diaminodiphenyl sulfone (DDS) or hexamethylenediamine (HMDA) into the carboxylic acid groups on GO *via* amide bonds. I prepared two kinds of mixtures, EP/DDS/DDS-GO and EP/DDS/HMDA-GO, by adding each diamine-functionalized GO as the co-curing agent into the mixture of diglycidyl ether of bisphenol-A (DGEBA)-type EP and 4,4′-diaminodiphenyl sulfone (DDS) curing agent (ca. 21 wt%). By increasing the amounts of DDS-GO from 0 to 1 wt%, the CD of EP/DDS/DDS-GO nanocomposite increased, and thus, I could effectively increase the T_g and tensile strength of EP nanocomposite.

2.2 Experiment

2.2.1 Materials

Graphite powder (average particle size < 30 ㎛), potassium permanganate (KMnO4), hexamethylenediamine (HMDA), and N,N′-dicyclohexylcarbodiimide (DCC) were purchased from Sigma-Aldrich Co. (USA). Sulfuric acid (H2SO4; 98%), hydrogen peroxide (H2O2; 30% in water), hydrochloric acid (HCl; 35% in water), and dichloromethane (DCM; 99.5%) were purchased by Daejung Chemical Co. (Korea). 4,4′-diaminodiphenyl sulfone (DDS) and 4-dimethylaminop-yridine (DMAP) were obtained from TCI Co. (Japan). Diglycidyl ether of bisphenol-A (DGEBA)-type EP resin (YD-128) was purchased from Kukdo Chemical Co. (Korea).

2.2.2 General procedure for synthesis of graphene oxide (GO)

GO was synthesized using the modified Hummer's method [31]. A round-bottom flask containing 98% H_2SO_4 (80 mL) was chilled to 0 ℃. Graphite powder (2 g) was added into the flask and stirred until mixed. $KMnO_4$ (10 g) was slowly added to the chilled graphite solution, and the resulting mixture was kept at 0 ℃. The mixture was then taken from the ice bath and stirred at 35 ℃ for 6 h. Deionized water (DI-water, 0.5 L) was slowly added, and the mixture was further stirred for 2 h. Subsequently, additional DI-water (1.5 L) was added followed by dropwise addition of 30% H_2O_2 (30 mL). The mixture was left undisturbed for 3 days for the precipitation to complete. The clear supernatant was decanted. The precipitate was repeatedly washed with DI-water followed by centrifugation with 20 ml of HCl solution (1 N), at least five times to remove residual metal oxides. The resulting GO dispersion was subjected to ultrasonication for 30 min, with occasional agitation at regular intervals of 10 min) for monolayer exfoliation. Dialysis was performed with a sealed membrane tube (Spectra/Por 1 Dialysis Tubing, MWCO 6-8,000) in DI-water with constant

stirring for 7 days. The DI-water was continuously exchanged every 3 h. After dialysis, the clear supernatant was removed by centrifugation at 10000 rpm for 30 min. After freeze-drying, deep-brown GO powder was obtained.

2.2.3 Synthesis of diamine-functionalized GO (diamine-GO)

A schematic representation of this process is shown in Scheme 2.1. All experiments were performed in an argon atmosphere. DCM was distilled prior to use. GO (0.1 g) and the diamine derivative (0.1 g) was added to DCM (200 mL) in a 500 mL flask, followed by ultrasonication for 60 min. After that, DCC and DMAP were added into the flask and ultrasonication was performed for 60 min. The number of moles of DCC and DMAP were the same as that of the diamine derivative. The reaction mixture was taken from the ultrasonicator and stirred at room temperature for 24 h. After the reaction, the mixture was washed with DCM, DI-water, and acetone, and filtered to remove excess diamine. The product was finally dried at 60 °C in vacuum for 24 h.

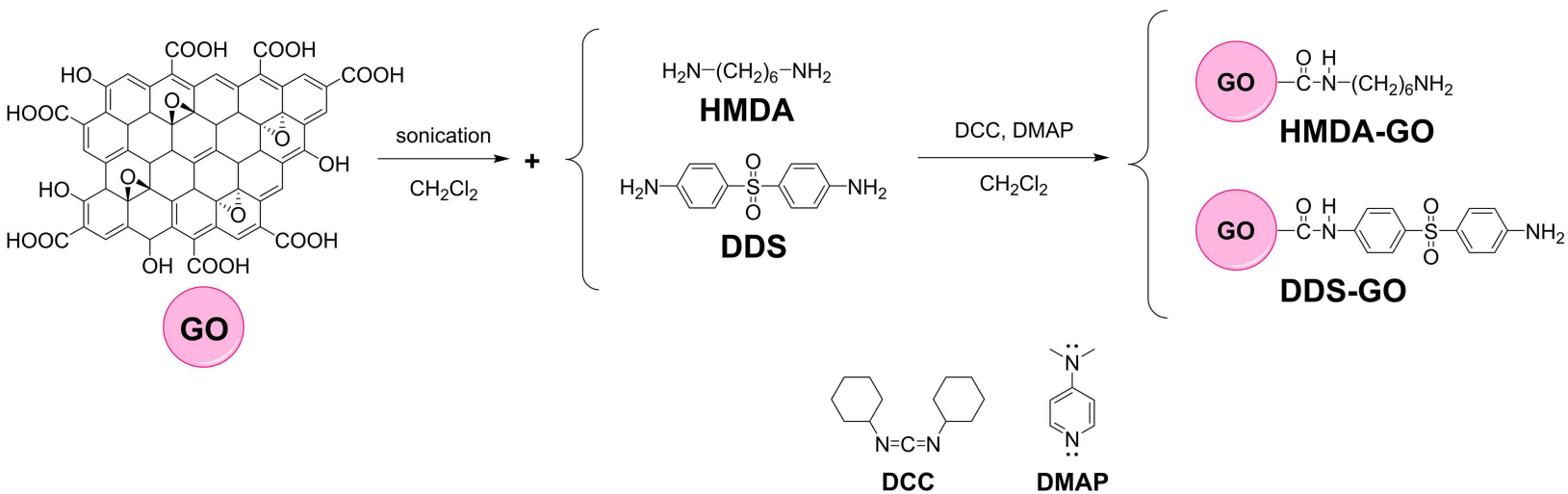

Scheme 2.1. **Synthetic routes for diamine-GO derivatives.**

2.2.4 Fabrication of epoxy nanocomposite

I calculated the approximately stoichiometric quantities of curing agent required for realizing optimum properties. The EP resin used in this study (DGEBA-type) has an epoxide equivalent weight (EEW) of about 185 g/eq. The viscosity is about 12,000 cP at 25 ℃. The curing agent used in this study, DDS, has an amine hydrogen equivalent weight (AHEW) of 62 g/eq. Stoichiometric amounts of the EP resin and curing agent were calculated according to the following formula because one N-H group reacts with one epoxide group.

$$Amount\,of\,curing\,agent = \frac{AHEW[g/eq] \times Amount\,of\,EP\,resin\,[g]}{EEW[g/eq]}$$

For example, the stoichiometric amount of DDS for 100 g of YD-128 was calculated to be 33 g. When diamine-GO was added in the nanocomposite, the mixing amount of curing agent reduced to 80% of the stoichiometric amount of DDS, because the amine groups on DDS-GO could also react with epoxide groups as a curing agent. The content of diamine-GO was calculated based on the entire amount of the EP resin and curing agent. EP/DDS/diamine-GO nanocomposites were prepared with different weight fractions of the diamine-GO (0.1 wt%, 0.5 wt%, and 1 wt%). More details on the mixing ratios for obtaining EP nanocomposites are shown in Table 2.1. The fabrication procedure for EP nanocomposites is as follows. Stoichiometric amounts of diamine-GO and EP resin were mixed using a planetary mixer with mixing speed of 2000 rpm for 10 min. After adding stoichiometric amount of DDS to the mixture of EP/amine-GO, the mixture was further mixed by stirring at 155 ℃ for 20 min. Then, the mixture was placed in vacuum to remove trapped air bubbles and poured into a mold, followed by precuring it in an oven at 170 ℃ for 4 h and curing at 230 ℃ for 2 h.

Tbale 2.1. Mixing ratios for obtaining EP nanocomposites

Samples	Components
Neat EP	EP (100 g) + DDS (33 g)
EP/DDS/GO 0.1 wt%	EP (100 g) + DDS (27 g) + GO (0.13 g)
EP/DDS/GO 0.5 wt%	EP (100 g) + DDS (27 g) + GO (0.66 g)
EP/DDS/GO 1.0 wt%	EP (100 g) + DDS (27 g) + GO (1.28 g)
EP/DDS/HMDA-GO 0.1 wt%	EP (100 g) + DDS (27 g) + HMDA-GO (0.13 g)
EP/DDS/HMDA-GO 0.5 wt%	EP (100 g) + DDS (27 g) + HMDA-GO (0.66 g)
EP/DDS/HMDA-GO 1.0 wt%	EP (100 g) + DDS (27 g) + HMDA-GO (1.28 g)
EP/DDS/DDS-GO 0.1 wt%	EP (100 g) + DDS (27 g) + DDS-GO (0.13 g)
EP/DDS/DDS-GO 0.5 wt%	EP (100 g) + DDS (27 g) + DDS-GO (0.66 g)
EP/DDS/DDS-GO 1.0 wt%	EP (100 g) + DDS (27 g) + DDS-GO (1.28 g)

2.2.5 Material characterization

The structural divergence of the GO and diamine-GO were confirmed by Fourier-transformation infrared spectroscopy (FT-IR; Nicolet iS 10, Thermo Scientific, USA). Thermogravimetric differential thermal analysis (TG-DTA) of the GO and diamine-GO were carried out with TA Q50 (TA Instrument, USA) under nitrogen gas flow at a heating rate of 10 ℃ per minute. X-ray photoelectron microscopy (XPS; AXIS-NOVA, Kratos Inc., USA) was employed to discern chemical changes on the surface of GO and diamine-GO. Al Kα (1485.6 eV) was used as the X-ray source at 14.9 keV anode voltage. 4.6 A and 20 mA were applied as the filament current and mission current, respectively. Atomic forced microscopy (AFM; Veeco-Digital Instruments, USA) images of the GO and diamine-GO were recorded to study morphologies. Optical microscopy (OM; Eclipse Ni, Nikon Inc, Japan) images of the GO and diamine-GO were used to evaluate the dispersion stability of DDS-GO in the EP nanocomposites. To investigate the thermal properties of EP nanocomposites, a differential scanning calorimeter (DSC; Q20, TA Instrument, USA) and a dynamic mechanical analyzer (DMA; Q800, TA Instrument, USA) were used. The DSC scanning temperature range was from 25 to 350 ℃ under nitrogen gas flow with a heating rate of 10 ℃ per minute. The DMA scanning temperature range was from 30 to 260 ℃ with a scanning rate of 3 ℃/min. The mechanical properties of nanocomposites were measured by using a universal testing machine (UTM; Instron, USA). The samples for UTM measurement were prepared with 1.5 mm thickness, 0.5 cm width, and 2.5 cm length, and the tensile strength test was performed at a testing speed of 5 mm/min.

2.3 Results and discussion

The carboxylic acid groups on GO and the amine groups were connected *via* amide covalent groups formed by the Steglich reaction [32]. Steglich esterification is the most common reaction for condensation of carboxylic acid and alcohol groups to form an ester group, and it is also very powerful to form an amide group from a carboxylic acid group and an amine group, which is more nucleophilic than the alcohol group. Successful condensation was confirmed by the appearance of amide groups determined *via* several analyses, as presented in Figure 2.1.

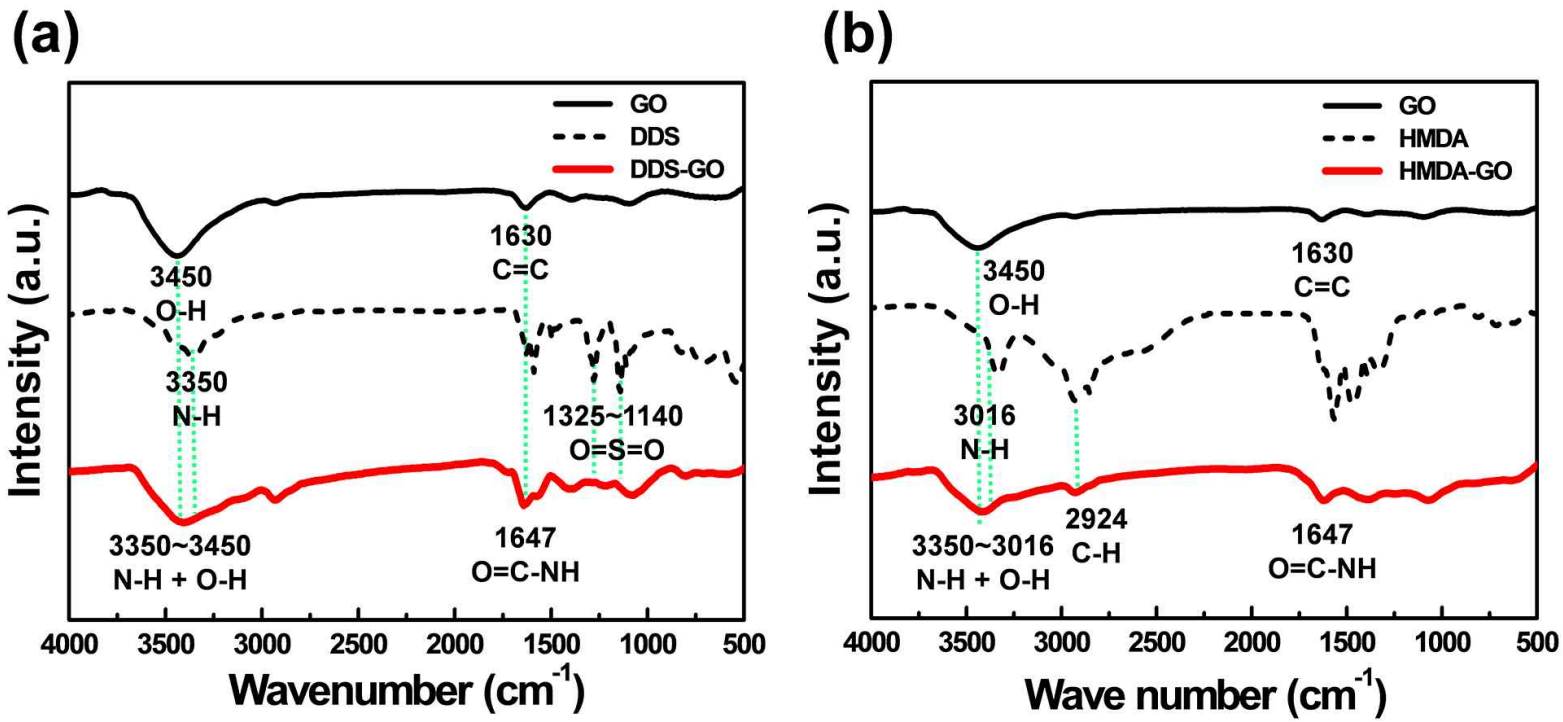

Figure 2.1. FT-IR spectra of (a) GO, DDS, and DDS-GO, and (b) GO, HMDA, and HMDA-GO

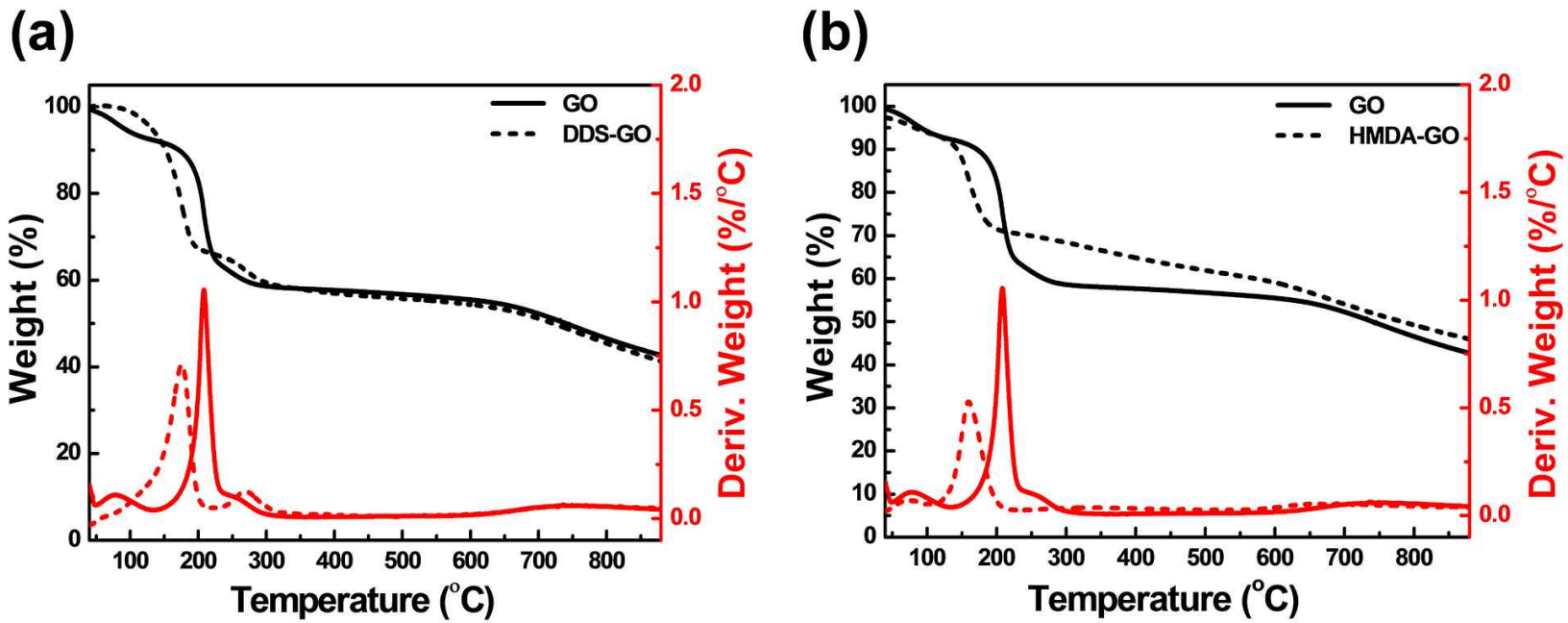

Figure 2.2. TG-DTA curves of (a) GO and DDS-GO, (b) GO and HMDA-GO during heating up to 900 °C in a N_2 atmosphere.

FT-IR analysis is an important technique to study the structural change in diamine-GO. Representative FT-IR spectra of DDS-GO are presented in Figure 2.1a to provide the proof of the successful synthesis of DDS-GO. FT-IR spectra of HMDA-GO are showed in figure 2.1b. There are three characteristic absorption bands in the FT-IR spectra of DDS-GO. First, an absorption band at 3450 cm^{-1} attributed to the O-H stretching vibration derived from O-H groups on GO [33]. This absorption band was quite broad, because the absorption band at about 3350 cm^{-1} assigned to N-H vibration of the amine group on DDS [34] combined with the O-H stretching vibration band of GO. Absorption bands corresponding to C=C skeletal vibration and C=O stretching vibration at 1630 cm^{-1} in the spectra of GO [33] and absorption bands of sulfone O=S=O stretching vibration at 1140–1325 cm^{-1} in the spectrum of DDS [34] also appeared in the FT-IR spectrum of DDS-GO. Meanwhile, a strong absorption band newly appeared at 1647 cm^{-1} in the spectrum of DDS-GO. I assigned it to the stretching vibration of the amide group created by condensation of the carboxylic acid group at the GO edge with the amine group of DDS [19]. These FT-IR analysis results are strong evidences of GO functionalization with the diamine derivatives.

Figure 2.2 shows the TG-DTA curves of GO, HMDA-GO and DDS-GO under a N_2 atmosphere. In the TG-DTA curve of GO, the small weight loss peak at 80 ℃ was due to the loss of residual water in GO, and the main weight loss peak that appeared around 210 ℃ is assigned to the pyrolysis of the labile oxygen functional groups, yielding CO, CO_2, and steam [35–36]. On the other hand, I could observe two different major loss peaks from the TG-DTA curve of DDS-GO. The peak near 160 ℃ could be ascribed to the loss of the remaining oxygen functional groups on GO, which slightly shifted to a temperature lower than that of non-functionalized GO. The peak around 270 ℃ corresponds to the decomposition of DDS [34]. From the decomposed weight, I calculated the substituted amount of DDS in DDS-GO as 7 wt%. With this method, the substituted amount of HMDA in HMDA-GO was also evaluated as 7 wt%. These results of TG-DTA analysis also indicate that diamine derivatives were

successfully introduced to GOs.

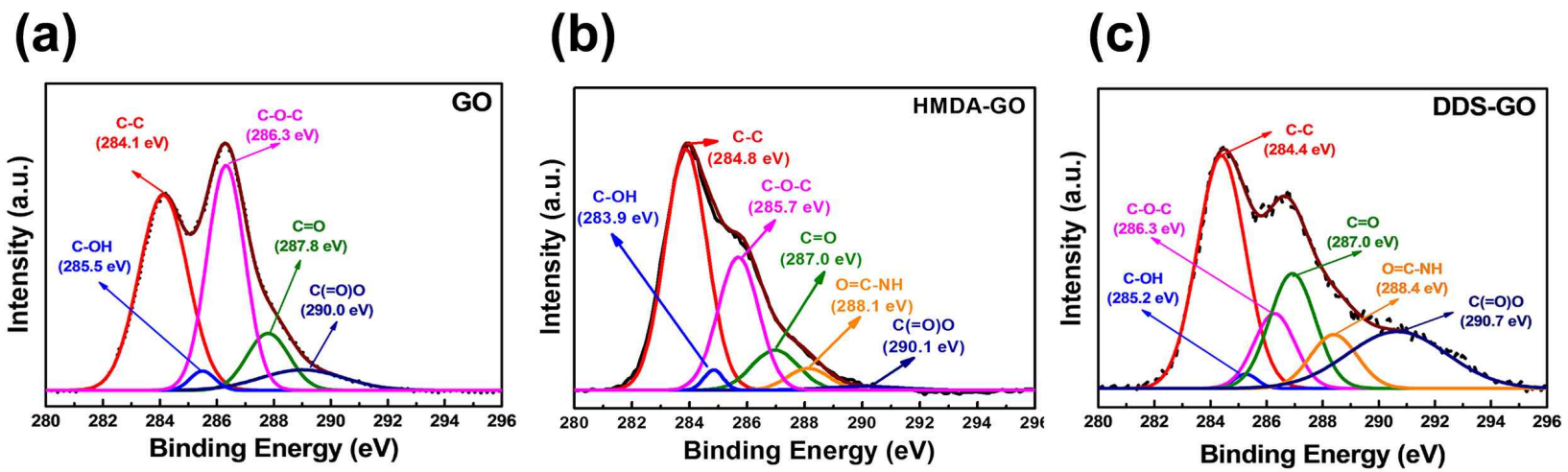

Figure 2.3. XPS C1s spectra of (a) GO, (b) HMDA-GO and (c) DDS-GO. Deconvoluted curves represent the theoretical XPS spectra for different chemical bonds.

Table 4.2. **XPS analysis results of diamine-GO**

Sample	XPS (%)					
	Carbon state					
	C-C	C-OH	C-O-C	C=O	O=C-NH	C(=O)O
GO	42.2	2.1	37.5	10.6	-	7.6
HMDA-GO	46.8	6.8	26.3	13.6	3	3.4
DDS-GO	39.5	1.8	12.4	19.1	9.0	6.9

Further investigation by XPS analysis was performed to characterize diamine-GOs, and the resulting deconvoluted XPS C1s spectra of GO, HMDA-GO, DDS-GO are shown in Figure 2.3. In Figure 2.2a, five characteristic peaks were observed at 284.4, 285.2, 286.3, 287.0, and 290.7 eV, which correspond to C-C, C-OH, C-O-C, C=O, and C(=O)-O, respectively. Further, an additional peak at 288.4 eV was observed in Figure 2.2b, c, and it could be assigned to O=C-NH moieties [37]. Integrated areas of the peaks corresponding to each chemical bond are listed in Table 2.2. From the existences of the O=C-NH peak in the XPS results, I found that amide groups were newly formed in the functionalized GO.

Thus, the results of FT-IR, TG-DTA, and XPS analyses confirmed that diamine derivatives were successfully introduced to GOs via amide chemical bonds.

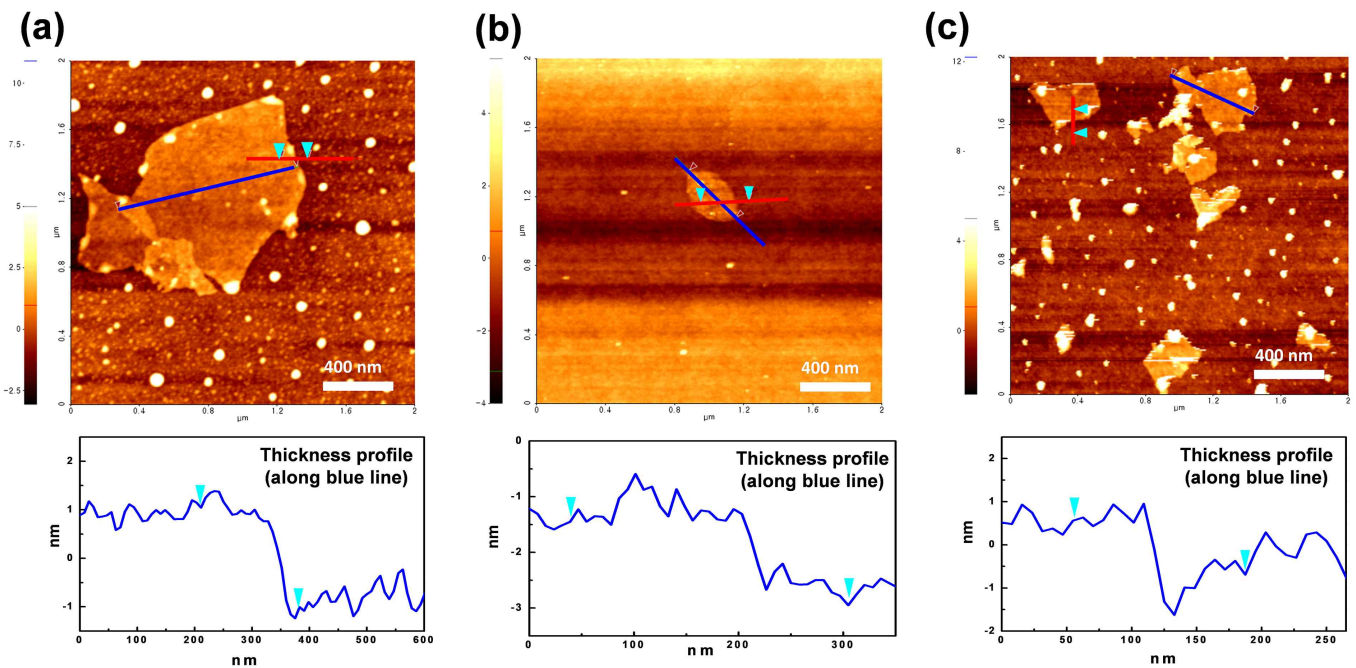

Figure 2.4. AFM images of (a) GO, (b) DDS-GO, and (c) HMDA-GO.

AFM analysis was employed to study morphologies of GO and diamine-GOs, and their images are in Figure 2.4. From these images, the presence of the nanolayer-type GO is clearly observed. The width and thickness of GO and diamine-GO were determined by the analysis results. The image of GO showed 2.0 nm of average thickness and 300–1100 nm width range. Further, images of DDS-GO and HMDA-GO revealed an average thickness of 1.0 nm and a width ranging from 100–500 nm. It is considered that the additional ultrasonication process in the case of the functionalized GO would shatter the GO into smaller pieces.

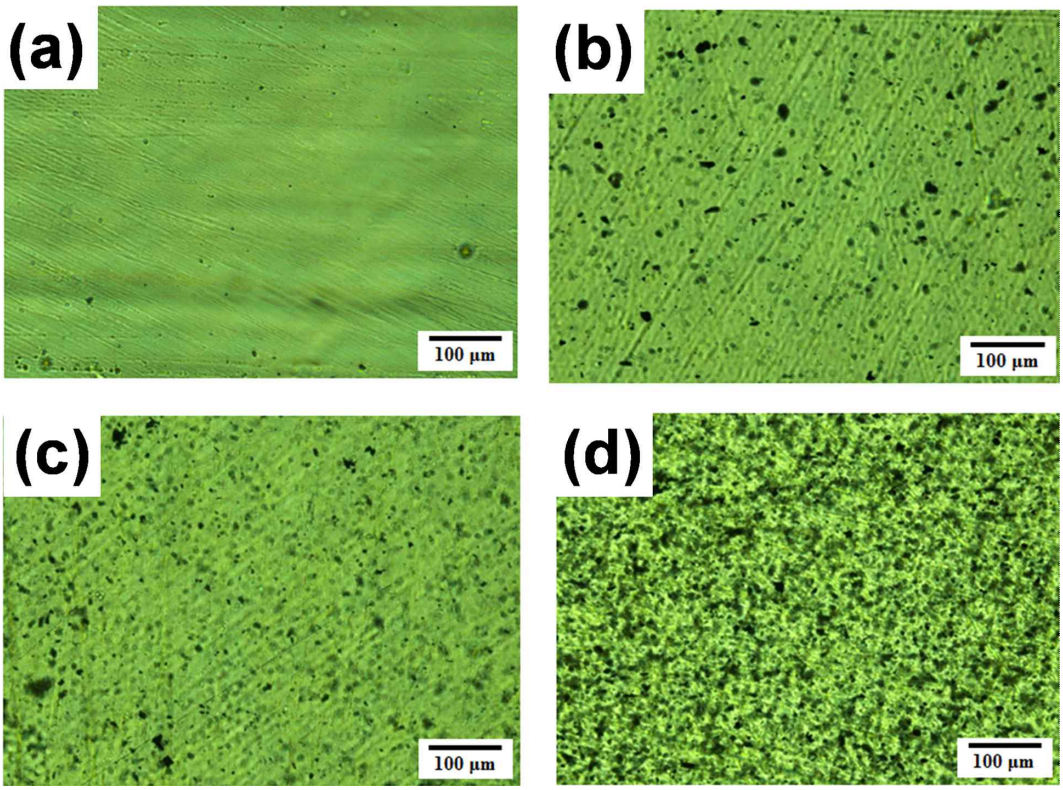

Figure 2.5 Optical microscope photographs of EP/DDS/DDS-GO nanocomposites as a function of weight percentage of DDS-GO. (a), (b), (c), and (d) correspond to 0, 0.1, 0.5, and 1.0 wt% of DDS-GO into the mixture of EP/DDS, respectively.

Good dispersion of nanomaterials greatly influences and improves the properties of the EP nanocomposites. Therefore, in order to investigate the dispersion state, EP/DDS/DDS-GO nanocomposites were observed by optical microscopy. The results are shown in the Figure 2.5, and they indicated that the DDS-GO dispersion in the EP nanocomposites was very homogeneous when the concentration was increased to 1.0 wt%. The presence of many polar moieties such as carboxylic acid, amide, and amine groups was thought to facilitate the dispersion of DDS-GO in the EP nanocomposite because they actively interact with EP *via* hydrogen or covalent bonding.

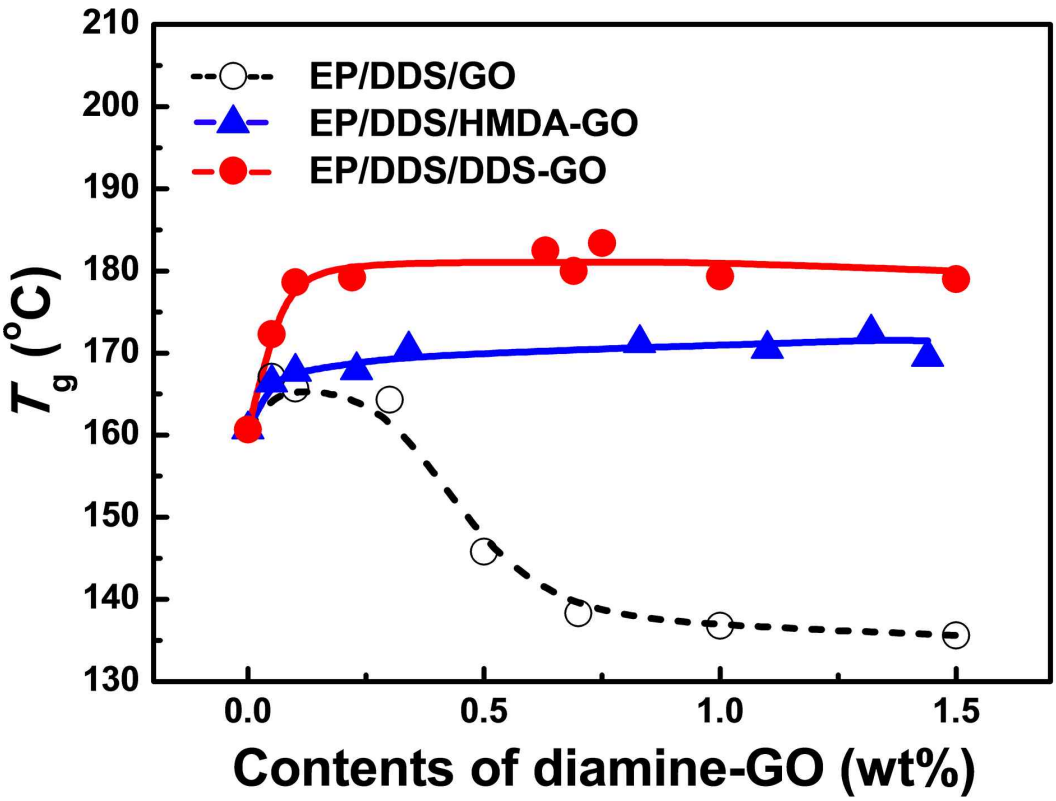

Figure 2.6. Glass transition temperatures (T_g) of EP/DDS/diamine-GO nanocomposites. T_g was estimated from the second heating DSC results of EP/DDS/diamine-GO mixture.

Table 2.3. **Curing temperatures of EP/DDS/diamine-GO nanocomposite**

wt%	0	0.05	0.1	0.3	0.5	0.7	1	1.5
GO	231	231.6	230.6	229.3	228.1	226.6	225.3	221.9
HMDA-GO	231	231.5	231.9	231.9	231.9	231.8	231.4	231.2
DDS-GO	231	231.8	232.3	233.2	234.2	235.4	234.6	235.4

Table 2.4. **Glass transition temperatures of EP/DDS/diamine-GO nanocomposites**

wt%	0	0.05	0.1	0.3	0.5	0.7	1	1.5
GO	231	231.6	230.6	229.3	228.1	226.6	225.3	221.9
HMDA-GO	231	231.5	231.9	231.9	231.9	231.8	231.4	231.2
DDS-GO	231	231.8	232.3	233.2	234.2	235.4	234.6	235.4

Addition of nanomaterials into the EP had a significant effect on the resulting thermal properties. As described in the Experimental section, diamine-GOs were used as co-curing agents of EP nanocomposites and their amount was controlled from 0.0 to 1.5 wt%. Curing temperatures were estimated from the temperatures of exothermic peaks in the first heating DSC curves of the EP/DDS/GO and EP/DDS/diamine-GO mixtures are presented in Table 2.3. T_g of the cured EP/DDS/GO and EP/DDS/diamine-GO nanocomposites were determined based on endothermic peaks of their second heating DSC curves (Figure 2.6, Table 2.4). When the GO was added to 1.0 wt% to the EP/DDS, the of the EP/DDS/DDS-GO nanocomposite decreased from 160.7 to 136.8 ℃. It has been reported that the non-functionalized GOs decrease of EP nanocomposites because of the tendency of GO to agglomerate in the polymer matrix and disturb polymer heat flow, but this tendency has not been investigated sufficiently [38]. In contrast, when 1.0 wt% of HMDA-GO or DDS-GO was added to the mixture of EP/DDS, the T_g of EP/DDS/diamine-GO nanocomposites remarkably increased to 170.5 or 183.4 ℃, respectively; these high values of obtained by adding HMDA-GO or DDS-GO are 125 and 135% of those for EP/DDS/GO nanocomposite, respectively. This is because the amine moieties functionalized on GO could improve the interfacial affinity by reacting with the epoxide groups of the EP resin. Subsequently, the disturbance of the interface between GO and EP could be reduced. If terminal amine groups on GO react with the epoxide groups of EP, diamine-GO could participate in the formation of a polymer crosslink network like curing agent, and EP/DDS/diamine-GO nanocomposites would show higher CD than the EP/DDS/GO nanocomposite. Further, it is known that the CD of EP nanocomposites is closely related to their thermal properties [21–22].

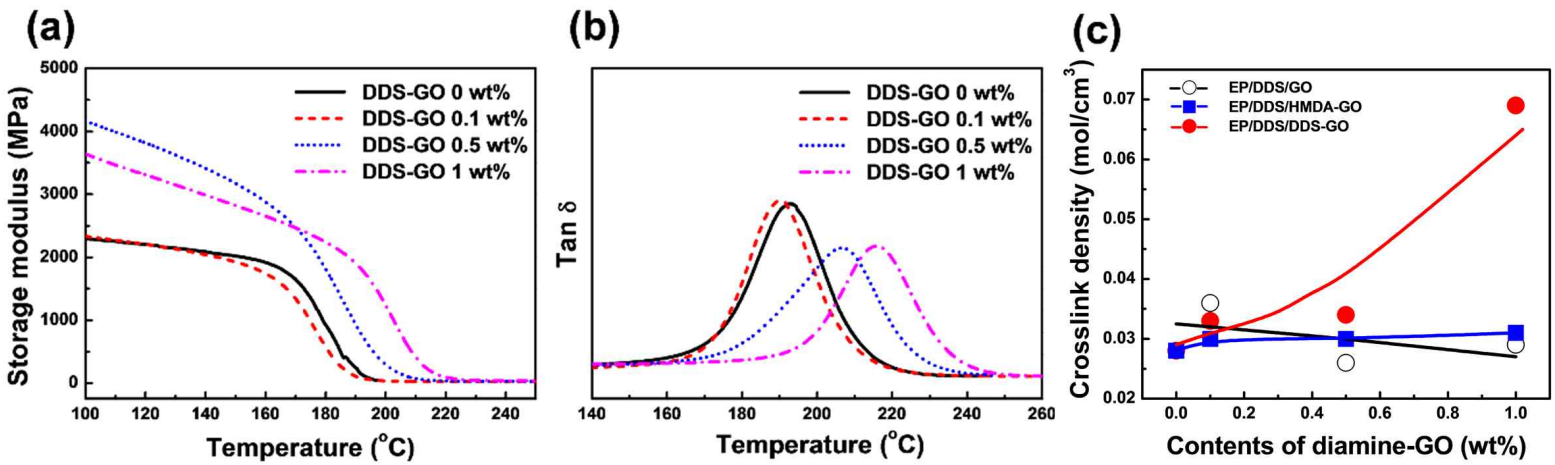

Figure 2.7. DMA results of EP/DDS/DDS-GO nanocomposites. (a) Storage modulus, (b) tanδ, and (c) crosslink density of the EP/DDS/DDS-GO nanocomposites. Samples were tested in a temperature range of 30 to 260 ℃ at a scanning rate of 3 ℃/min. The crosslink density was calculated using storage modulus and tanδ in the rubbery region of EP/DDS/diamine-GO nanocomposites.

***Table 2.5*. Crosslink densities (CD) of the EP/DDS/diamine-GO nanocomposites**

Additive (Contents)	Crosslink density [mol/cm^3]
Neat EP (0.0 wt%)	0.028
GO (0.1 wt%)	0.036
GO (0.5 wt%)	0.026
GO (1.0 wt%)	0.029
HMDA-GO (0.1 wt%)	0.030
HMDA-GO (0.5 wt%)	0.031
HMDA-GO (1.0 wt%)	0.031
DDS-GO (0.1 wt%)	0.033
DDS-GO (0.5 wt%)	0.034
DDS-GO (1.0 wt%)	0.069

DMA measurements of EP/DDS/GO nanocomposites and EP/DDS/DDS-GO nanocomposites were performed to estimate the CD of EP nanocomposites. Storage modulus and tanδ of EP/DDS/DDS-GO nanocomposites are shown in Figure 2.6a-b. Based on the storage modulus and tanδ in the rubber region, CD of EP nanocomposites were calculated according to the following formula [30]:

$$\rho = \frac{G'}{RT}$$

where ρ is the CD in mol/cm^3, G' is the shear modulus calculated from the storage modulus measured in the rubbery region of EP nanocomposites, R is a universal gas constant (8.314472 J/K•mol), and T is the absolute temperature at which G' was determined. The results of calculated crosslink densities are shown in Figure 2.7c and Table 2.5. The CD of EP/DDS/GO and EP/DDS/HMDA-GO nanocomposites did not changed much from that of neat EP. However, the CD of EP/DDS/DDS-GO nanocomposite showed significant enhancement as the contents of DDS-GO increased. In particular, when 1.0 wt% of DDS-GO was incorporated, the CD of EP/DDS/DDS-GO nanocomposites was 0.069 mol/cm^3, and this is 240% of the CD of cured EP (0.028 mol/cm^3). Amine terminal groups attached to the DDS-GO could react with the epoxide groups of the EP and construct the crosslink network through covalent bonds on the interface between GO and EP. Therefore, the CD of EP/DDS/DDS-GO nanocomposite became higher than that of the EP/DDS/GO nanocomposite, and the former showed superior thermal properties.

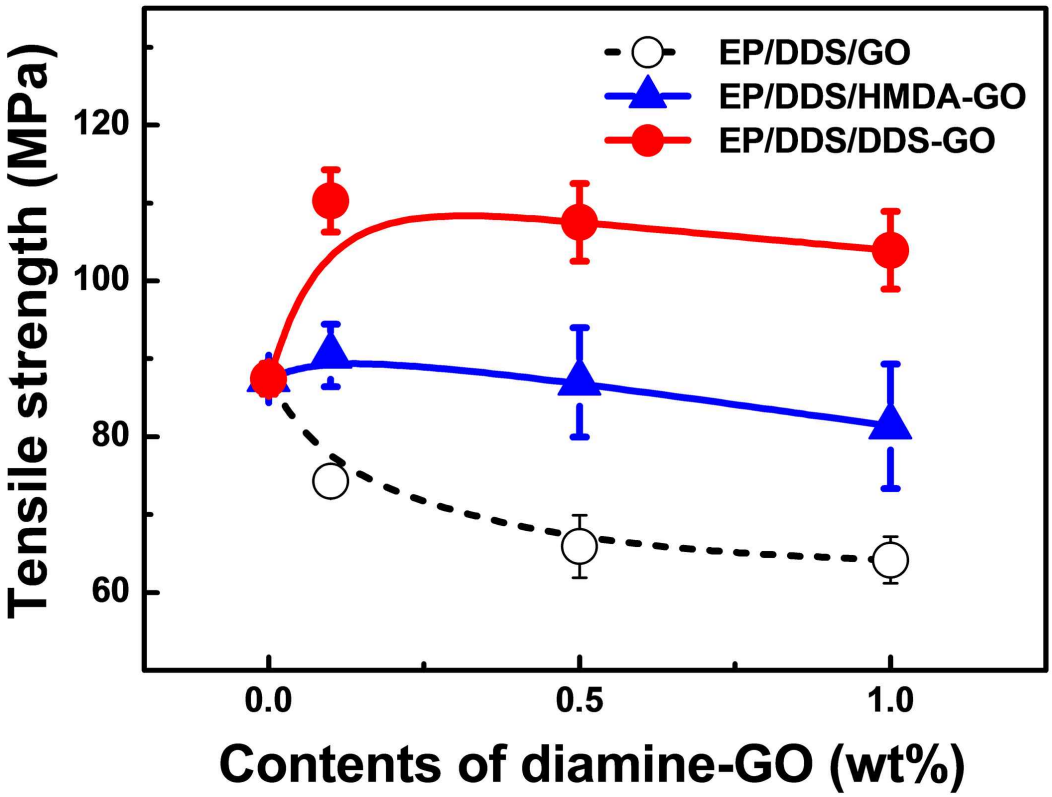

Figure 2.8. Tensile strengths of EP/DDS/diamine-GO nanocomposites. It was estimated by using a universal testing machine. Samples for measurement were prepared with 1.5 mm × 50 mm × 250 mm size, and tests were performed with a testing speed of 5 mm/min.

It has been also known that CD is not only related to the thermal properties of EP nanocomposite, but also related to the mechanical properties [23–24]. In order to investigate the effect of CD on the mechanical properties of EP nanocomposite, the tensile strength of EP/DDS/diamine-GO nanocomposites was evaluated by UTM analysis; an analysis result is shown in Figure 2.8. Similar to the T_g, the tensile strength of EP/DDS/DDS-GO nanocomposite was higher (110.3 MPa) than those of neat EP (87.4 MPa) and the EP/DDS/GO nanocomposite (74.3 MPa) when 0.1 wt% of DDS-GO or GO was added. The EP/DDS/HMDA-GO nanocomposite also showed the higher tensile strength (90.4 MPa) compared to those of neat EP and the EP/DDS/GO nanocomposite, but the amount increase was relatively small. In the EP/DDS/diamine-GO nanocomposite, diamine-GO could have strong interactions with EP through covalent bonds between diamine-GO and EP, and this is considered to be the reason for the improvement in the tensile strength of the EP/DDS/diamine-GO nanocomposite.

Meanwhile, both EP/DDS/HMDA-GO and EP/DDS/DDS-GO nanocomposites showed higher Tg and tensile strength values than the EP/DDS/GO nanocomposite, but the EP/DDS/DDS-GO nanocomposite exhibited superior properties to the EP/DDS/HMDA-GO nanocomposite. We thought that this result was due to the structural difference between HMDA, which has a flexible aliphatic structure, and DDS, which has a rigid aromatic sulfone structure. In the case of HMDA-GO, terminal amine groups are connected with GO through a flexible alkyl chains, and these may affect the lower Tg and tensile strength of EP/DDS/HMDA-GO nanocomposite than that of EP/DDS/DDS-GO nanocomposite. In addition, terminal amine groups with different nucleophilicity exist. These terminal amine groups act as curing sites and are considered to be major factors that affect the thermal and mechanical properties of EP nanocomposites. HMDA has electron-rich aliphatic amine groups which can make the curing temperature of HMDA-GO lower than that of the main curing agent DDS.

Consequently, a spatially heterogeneous curing reaction will take place in the nanocomposite, and this could negatively affect the thermal properties of EP/DDS/HMDA-GO. In contrast, DDS-GO starts to participate in curing at a similar temperature as DDS. Therefore, the curing reaction would occur more homogeneously in the EP/DDS/DDS-GO nanocomposite, and the thermal properties would be better. This hypothesis about the difference between HMDA-GO and DDS-GO was supported by the CD of EP/DDS/HMDA-GO, which was much lower than that of EP/DDS/DDS-GO. Moreover, the EP/DDS/DDS-GO nanocomposite showed increasing CD when the more DDS-GO was added, while the CD of EP/DDS/HMDA-GO nanocomposite did not changed much despite the high contents of HMDA-GO.

2.4 References

[1] A. M. Atta, N, O. Shaker, N. E. Nasser, *J. Appl. Polym. Sci.* 107, 347 **(2008).**

[2] V. Dixit, A. K. Nagpal, R. Singhal, *Int. J. Plast. Technol.* 14, 38 **(2010).**

[3] T. Song, Z. Li,; J. Liu, S. Yang, *Polym. Sci. Ser. B*, *55*, 147 **(2013).**

[4] B. J. P. Jansen, K. Y. Tamminga, H. E. H. Meijer, P. J. Lemstra, *Polymer*, 40, 5601 **(1999)**.

[5] T. V. Kosmidou, A. S. Vatalis, C. G. Delides, E. Logakis, P. Pissis, G. C. Papanicolaou, *eXPRESS Polym. Lett.* 2, 364 **(2008).**

[6] Abdalla, M.; Dean, D.; Theodore, M.; Fielding, J.; Nyairo, E.; Price, G. *Polymer,* 51, 1614 **(2010).**

[7] M. M. Rahman, S. Zainuddin, M. V. Hosur, C. J. Robertson, A. Kumar, J. Trovillion, S. Jeelani, *Compos. Struct.* 95, 213 **(2013).**

[8] J. Zhu, S. Wei, J. Ryu, M. Budhathoki, G. Liang, Z. Guo, *J. Mater. Chem.* 20, 4937 **(2010).**

[9] L. Tang, Y. Wan, D. Yan, Y. Pei, L. Zhao, Y. Li, L. Wu, J. Jiang, G. Lai, *Carbon* 60, 16 **(2013).**

[10] J. A. King, D. R. Klimek, I. Miskioglu, G. M. Odegard, *J. Appl. Polym. Sci.* 128, 4217 **(2013).**

[11] A. S. Wajid, H. S. T. Ahmed, S. Das, F. Irin, A. F. Jankowski, M. J. Green, *Macromol. Mater. Eng.* 298, 339 **(2013).**

[12] Q. Li, Y. Guo, W. Li, S. Qiu, C. Zhu, X. Wei, M. Chen, C. Liu, S. Liao, Y. Gong, A. K. Mishra, L. Liu, *Chem. Mater.* 26, 4459 **(2014).**

[13] T. Ramanathan, A. A. Abdala, S. Stankovich, D. A. Dikin, M. Herrera-Alonso, R. D. Piner, D. H. Adamson, H. C. Schniepp, X. Chen, R. S. Ruoff, S. T. Nguyen, I. A. Aksay, R. K. Prud'homme, L. C. Brinson, *Nat. Nanotechnol.* 3, 327 **(2008).**

[14] T. Kuilla, S. Bhadra, D. Yao, N. H. Kim, S. Bose, J. H.Lee, *Prog. Polym. Sci.* 35, 1350 **(2010).**

[15] C. Bao, Y. Guo, L. Song, Y. Kan, X. Qian, Y. Hu, *J. Mater. Chem.* 21, 13290 **(2011).**

[16] B. Qi, S. R. Lu, X. E. Xiao, L. L. Pan, F. Z. Tan, J. H. Yu, *eXPRESS Polym. Lett.* 8, 467 **(2014).**

[17] B. Qi, Z. Yuan, S. Lu, K. Liu, S. Li, L. Yang, J. Yu, *Fiber. Polym.* 15, 326 **(2014).**

[18] M. M. Gudarzi, F. Sharif, *eXPRESS Polym. Lett.* 6, 1017 **(2012).**

[19] T. Liu, Z. Zhao, W. W. Tjiu, J. Lv, C. Wei, *J. Appl. Polym. Sci.* 131, 40236 **(2014).**

[20] L. Guan, Y. Wan, L. Gong, D. Yan, L. Tang, L. Wu, J. Jiang, G. Lai, *J.*

Mater. Chem. A, 2, 15058 **(2014).**

[21] T. Iijima, N. Yoshioka, M. Tomoi, *Eur. Polym. J.* 28, 573 **(1992).**

[22] K. W. Putz, M. J. Palmeri, R. B. Cohn, R. Andrews, L. C. Brinson, *Macromolecules* 41, 6752 **(2008).**

[23] K. Kim, I. Jeon, S. Ahn, Y. Kwon, J. Baek, *J. Mater. Chem.* 21, 7337 **(2011).**

[24] K. Wei, G. Zhu, Y. Tang, T. Liu, J. Xie, *J. Mater. Res.* 28, 2903 **(2013).**

[25] V. Patil, R. V. Dennis, T. K. Rout, S. Banerjee, G. D. Yadav, *RSC Adv.* 4, 49264 **(2014).**

[26] G. Z. Li, L. Wang, H. Toghiani, T. L. Daulton, K. Koyama, C. U. Jr. Pittman, *Macromolecules* 34, 8686 **(2001).**

[27] J. Park, S. C. Jana, *Macromolecules* 36, 8391 **(2003).**

[28] W. Naous, X. Yu, Q. Zhang,; Naito, K.; Kagawa, Y. *J. Polym. Sci. Polym. Phys.* 44, 1466 **(2006).**

[29] M. S. Lakshmi, B. Narmadha, B. S. R. Reddy, *Polym. Degrad. Stab.* 93, 201 **(2008).**

[30] C. Lee, J. Park, *Trans. Electr. Electron. Mater.* 11, 69 **(2010).**

[31] W. S. Hummers, R. E. Offeman, *J. Am. Chem. Soc.* 80, 1339 **(1958).**

[32] B. Neises, W. Steglich, *Angew. Chem. Int. Ed. Eng.* 17, 522 **(1978).**

[33] L. Shahriary, A. A. Athawale, *Int. J. Renew. Energy Environ. Eng.* 2, 58 **(2014).**

[34] L. Jiang, Y. Huang, Q. Zhang, H. He, Y. Xu, X. Mei, *Cryst. Growth Des.* 14, 4562 **(2014).**

[35] S. Stankovich, D. A. Dikin, R. D. Piner, K. A. Kohlhaas, A. Kleinhammes, Y. Jia, Y. Wu, S. T. Nguyen, R. S. Ruoff, *Carbon* 2007, 45, 1558 **(2007).**

[36] X. Du, Z. Yu, A. Dasari, J. Ma, M. Mo, Y. Meng, Y. Mai, *Chem. Mater.* 20, 2066 **(2008).**

[37] Y. Chen, X. Zhang, P. Yu, Y. Ma, *Chem. Commun.* 30, 4527 **(2009).**

[38] N. Norhakim, S. H. Ahmad, C. H. Chia, N. M. Huang, *Sains Malays.* 43, 603 **(2014).**

Chapter 3.

Conclusion

I successfully prepared diamine-functionalized graphene oxides (diamine-GOs), by introducing diamine derivatives at GO edge. The formation of amide groups was confirmed by several analyses such as FT-IR, TG-DTA, and XPS. EP nanocomposites obtained using diamine-GOs as co-curing agents of commercially available EP showed significantly improved thermal and mechanical properties compared to those of neat EP. In particular, 4,4′-diaminodiphenyl sulfone-functionalized GO (DDS-GO) was the most effective additive: 0.1 wt% content of DDS-GO enhanced the of EP/DDS/DDS-GO nanocomposite from 160.7 ℃ for EP to 183.4 ℃ and the tensile strength from 87.4 MPa for EP to 110.3 MPa. The improvement in properties was considered to be due to the good dispersion of DDS-GO in the EP/DDS/DDS-GO nanocomposite and the increase in the crosslink density (CD) of the EP/DDS/DDS-GO nanocomposite. Thus, I can improve the CD value of EP/DDS from 0.028 to 0.069 mol/cm^3 by adding 1.0 wt% of DDS-GO. Higher CD value was achieved for EP/DDS/DDS-GO because DDS-GO has terminal amine groups that tend to participate in the formation of crosslink network *via* direct covalent bonding with epoxide groups of EP. It is expected that the high-performance EP nanocomposite could be prepared by improving the CD of EP nanocomposites, and the method in this study could provide great potential to future industrial applications.

Chapter 4.
Appendix

Synthesis of twisted ribbon-like carbon, carbon microtubes and carbon rod from mercerized cotton fiber

1. Abstract

I used mercerized cotton fibers as carbonization precursors to fabricate carbon materials having different structures. The morphologies of the synthesized carbon materials were successfully controlled by varying the mercerization time. Twisted ribbon-like carbon structures, carbon microtubes, and carbon rods could be synthesized by carbonizing non-mercerized cotton fibers, cotton fibers mercerized for 40 min, and fully mercerized cotton fibers (i.e., fibers mercerized for 60 min), respectively. Interestingly, along with the morphological changes, the specific surface areas of these carbon materials were also changed to 203.7, 726, and 276.7 m^2/g, respectively. This method of fabricating carbon materials should lead to the synthesis of novel, structured carbon materials with various functionalities as it exploits both the natural structure of cotton fibers and artificial chemical processes.

2. Introduction

Many of the unique and exquisite hierarchical structures found in nature are still difficult to synthesize artificially. Cellulose, which is the most abundant material in the biosphere, is the primary constituent of wood and plants. It has a unique nanostructure that allows it to perform important life-sustaining functions. Natural structures such as that of cellulose have provided compelling insights and are proving to be of great use in various applications. For example, highly porous carbon materials were successfully manufactured from porous coconut shells [1]. Further, a metal microcoil was fabricated using a helically structured vascular plant [2].

Cotton fibers (CtFs) consist of a cuticle, a primary wall, a secondary wall, and a lumen. Most of the cellulose exists in the primary and secondary walls. Many hundreds of celluloses gather and form microfibrils. The primary and secondary walls of CtF consist of a number of microfibrils wrapped around the fiber axis. The lumen, which is located in the center of the secondary wall, is a hollow channel that carries nutrients for growth [3]. A cotton fiber has natural twists along its entire length; these are called convolutions. Interestingly, the shapes of the lumen and the convolutions are chemically changeable by treating the fibers with a high-concentration aqueous sodium hydroxide solution. This process is called mercerization [4]. Mercerization has been employed in the cotton industry to prevent cotton fabric from shrinking and to give it a lustrous appearance [5].

Recently, cellulose was used as a carbonization precursor after being heat treated at a high temperature [6,7]. If one could use mercerized CtF as a carbonization precursor while ensuring that they retain their morphology even after their conversion to a carbon material, it would become possible to use them to synthesize microtube-like carbon materials. It is likely that I could easily produce carbon microtubes by using exploiting both the natural structure of CtF and chemical modification methods.

3. Experiment

Cotton yarn was purchased from a commercial source, and CtF was prepared from the yarn. Mercerization was performed by dipping the CtF into a 15 wt% aqueous NaOH solution. The CtF were soaked at room temperature for 10, 20, 40, or 60 min, and washed with the deionized (DI) water. The mercerized CtF (M-CtF) subjected to the alkaline treatment for 10, 20, 40, and 60 min are referred to as M-CtF(10), M-CtF(20), M-CtF(40), and M-CtF(60), respectively. Next, samples of the M-CtFs were neutralized by being dipped into a 5 wt% aqueous HCl solution. The neutralized M-CtF were washed with DI water and dried for 12 h at room temperature. The carbonization of the CtF and M-CtF samples was performed using an electric furnace (KDF75, Denken Co., Ltd, Japan). The CtF and M-CtF samples were heated to 800 ℃ at a heating rate of 10 ℃/min and then were kept at 800 ℃ for 1 h under flowing argon gas. After the completion of the carbonization process, the electric furnace was allowed to cool to room temperature, and the samples were removed from the furnace. The carbonized CtF and M-CtF samples are referred to as C-CtF and CM-CtF, respectively. The morphologies of M-CtF and CM-CtF were observed using field-emission scanning electron microscopy (FESEM) (Nova NanoSEM 450, FEI Co., USA). The crystallinities of the porous carbon materials were investigated using transmission electron microscopy (TEM) (Tecnai G2 F20, FEI Co., USA). An elemental analyzer (vario MICRO cube, Elementar Analysensysteme, Germany) was used to analyze the changes in the elemental contents of the CM-CtF samples. The porosities of the samples were determined through N_2 adsorption analyses performed at 77 K using a volumetric adsorption measurement system (BELSORP-max, BELJapan, Inc., Japan); the system was pre-evacuated for 6 h at 573 K and 10^{-4} Pa. The electrical conductivities of the sample swere measured using the four-point probe method (FPP-RS8, Dasol Engineering Co., Ltd., Korea). The distance between the electrodes was 2 cm,

and each sample type was tested 30 times.

4. Results and Discussion

The changes in the morphology of the CtF during mercerization were examined using SEM (Figure 1). Before mercerization, the CtF exhibited a flat and twisted, ribbon-like structure, as can be seen in Figure 1a; as noted previously, such structures are called convolutions. The cross section has a distorted, bean-like shape. Further, crushed lumens can be seen between the sandwiched secondary walls in the inset of Figure 1a. During the mercerization process, the most significant shape changes were seen in the cross sections of the CtF. Further, convolutions were formed, the lengths of the CtF decreased, and their diameters increased. With an increase in the mercerization time, the twisted convolutions gradually disappeared. The cross sections deformed and became oval shaped after mercerization for 10 min (see Figure 1b). Moreover, the hollow-channeled lumens also became oval. After mercerization for 40 min, the oval-shaped cross sections became almost round, and the convolutions became disentangled (see Figure 1c). Further, the structures of the squashed lumens also changed, and the lumens became round. Finally, in M-CtF(60), which were mercerized for 60 min, the hollow channel shrank and disappeared (Figure 1d). As a result, the ribbon-like CtF transformed gradually into oval and round tubes, eventually becoming round rods, during the mercerization process.

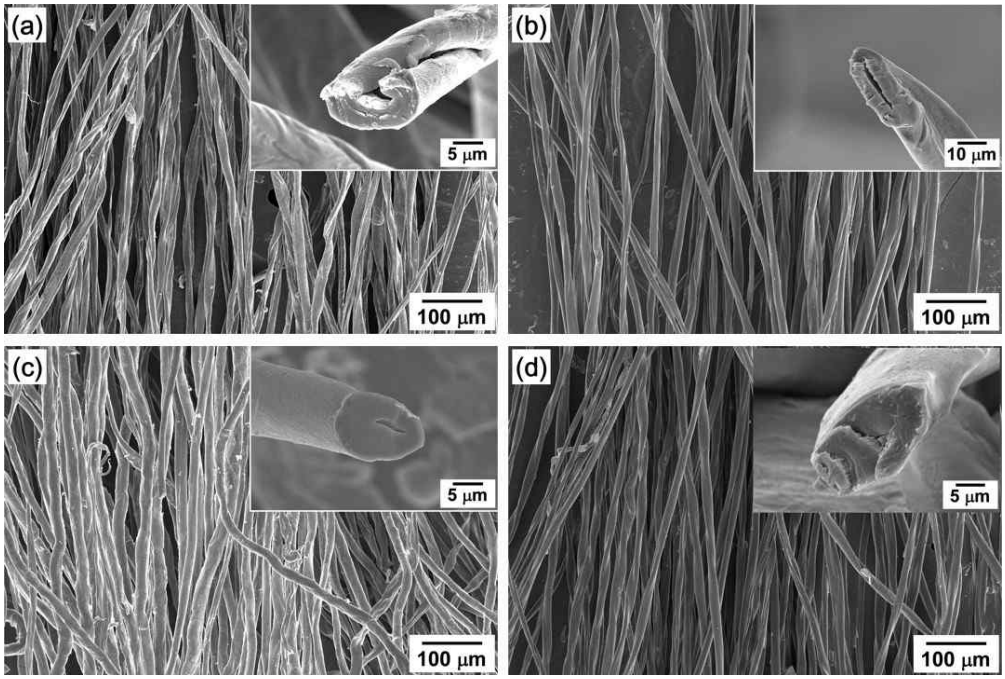

Figure 1. **SEM images of the (a) CtF and (b-d) M-CtF samples: (b) mercerization time of 10 min; (c) mercerization time of 40 min; and (d) mercerization time of 60 min.**

Thermogravimetric/differential thermal analyses (TG-DTA) of the CtF and M-CtF samples were performed using a TA Q50 system (TA Instruments, USA) under a flow of nitrogen gas at a heating rate of 5 ℃/min. Figure 2 shows the TG and DTA curves of CtF and M-CtF(40). All the samples exhibited a small degree of weight loss in the low-temperature range, that is, for temperatures below 110 ℃; this was owing to the evaporation of the water in the samples. During the heating process, all samples exhibited primary decomposition peaks at 200–400 ℃, as can be seen from the DTA curves. However, there was a difference in the maximum decomposition temperatures of CtF and M-CtF(40), which were 335 and 355 ℃, respectively. This difference may be related to the differences in the crystallinities or crystal structures of the CtF and M-CtF samples. It is rationalized that sodium hydroxide breaks the hydrogen bonds between the different cellulose types, causing the crystalline part of cellulose to swell during the mercerization process. After the completion of the mercerization process, the lattice of the crystal structure of the CtF transformed from the cellulose-I type to the cellulose-II type [8]. X-ray diffraction (XRD) analyses were used to examine the crystal structures of CtF and M-CtF(40). The XRD patterns and profiles were determined through two-dimensional X-ray diffraction (2D XRD) analyses (D8 Discover, Bruker Co., Germany); the XRD patterns were obtained on flat film using a sample holder at room temperature. The X-ray power was set at 16 kW. The XRD profiles of CtF and M-CtF(40) are shown in Figure 3. It was found that the pattern of CtF exhibited two strong diffraction peaks in the large-angle region (2θ = 22°); this could be assigned to cellulose II and in the small-angle region (2θ = 15.5°); this was assignable to cellulose I (Figure 3a) [8-10]. However, the XRD profile of M-CtF(40) exhibited a strong diffraction peak in the large-angle region (2θ = 22°) and weak diffraction peak in the small-angle region (2θ = 15.5°) (Figure 3b). These results indicated that the structure of most of the crystals transformed into the cellulose-II type; however, cellulose I remained in a small amount even after mercerization for 40 min. This would also have an

effect on the thermal decomposition behavior of CtF. After thermal decomposition at temperatures greater than 800 ℃, less than 7.3 and 13.8 wt% of the CtF and M-CtF(40) samples, respectively, remained, as can be seen from the A curves.

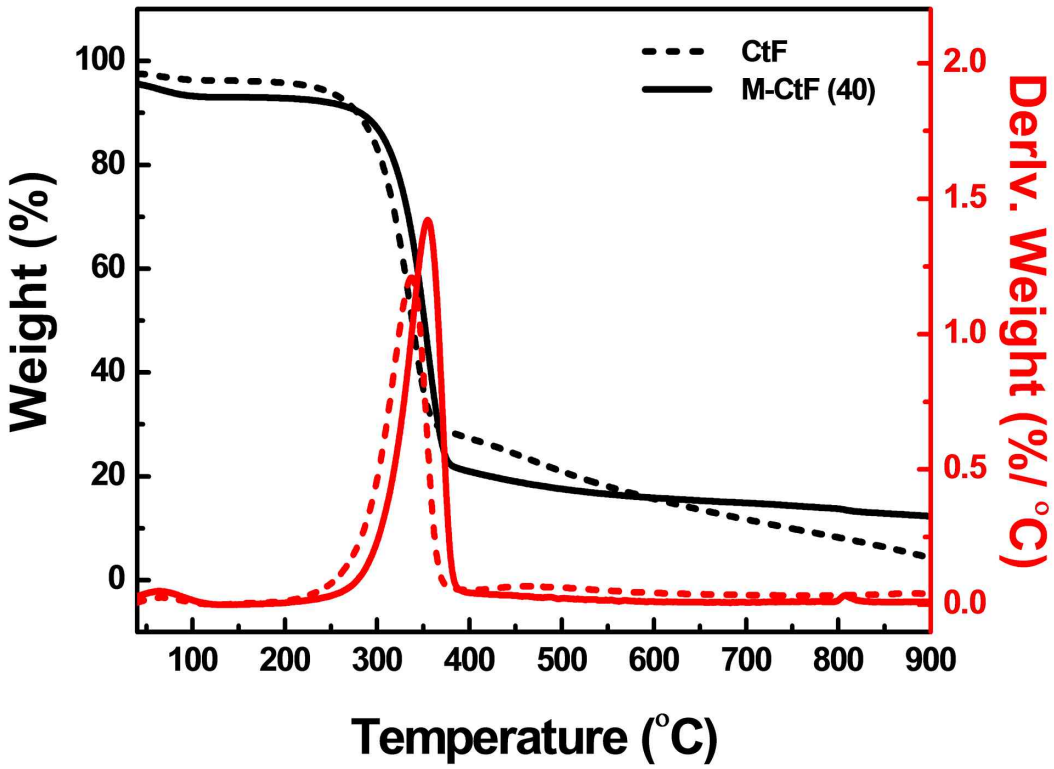

Figure 2.. A TG and DTA curves of CtF and M-CtF(40).

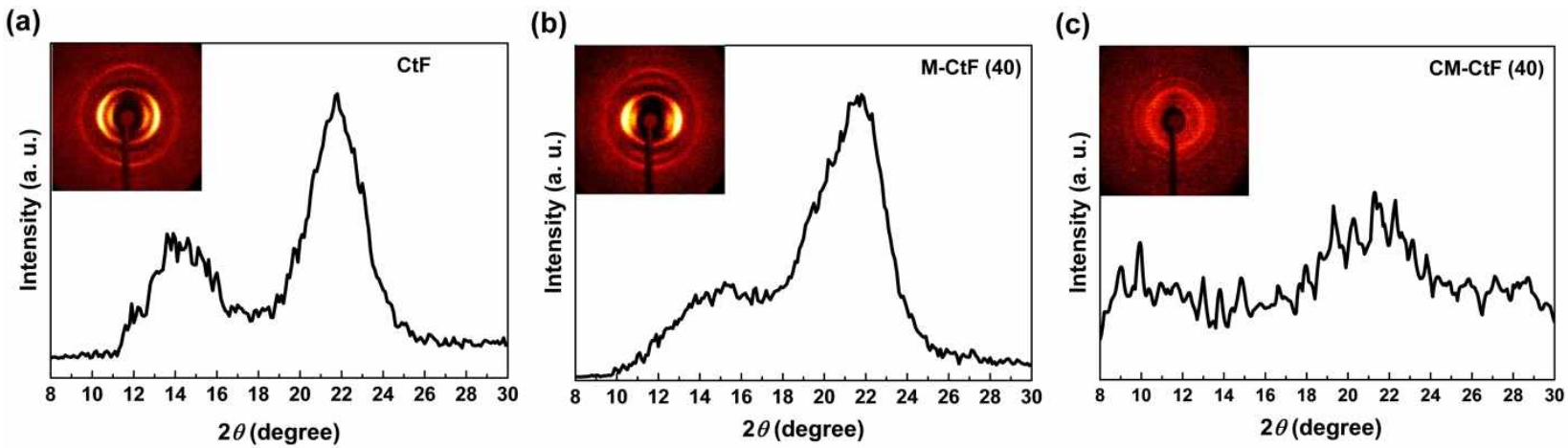

Figure 3. (a) XRD profiles of CtF, M-CtF(40) and (b) CM-CtF(40). The insets are 2D diffraction patterns of CtF, M-CtF(40) and CM-CtF(40).

The CtF and M-CtF samples were carbonized at 800 ℃ (see more detailed carbonization process in experimental). The carbonization yields of the C-CtF and CM-CtF samples were determined to be approximately 10% and 15%, respectively. The elemental analyses of the CM-CtF samples indicated that they consisted of 93.62% carbon, 1.32% hydrogen, and 2.71% oxygen. Using Raman spectroscopy, the ratio of the intensity of the peak corresponding to the graphite lattice (G-band), observed at 1575 cm−1,and the disorder band (D-band), noticed at approximately 1355 cm^{-1}, (i.e., I_D/I_G,) of CM-CtF (40) was found to be 0.98 (Figure 4). From the XRD measurement, I confirmed that the cellulose structures are disappeared completely, and graphitic structures were noticed (Figure 3c) [11].

Very interestingly, the shapes of the CtF and M-CtF samples remained unchanged even after carbonization at 800 ℃ (Figure 5). With an increase in the mercerization time, the distorted bean-like cross section of C-CtF became oval and round. In addition, the narrow and crushed lumens of C-CtF also changed, becoming round. A fully extended, hollow channel was seen in the case of CM-CtF(40). However, the lumens were closed in CM-CtF(60).

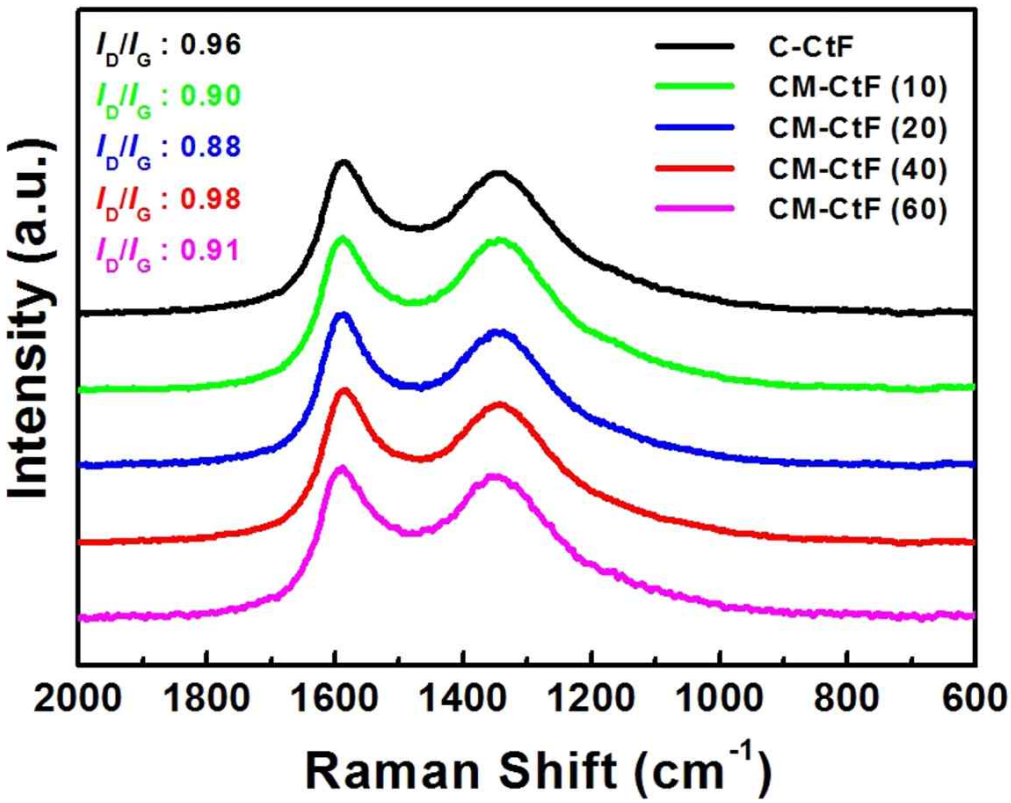

Figure 4. Raman spectra of CtF and CM-CtF sample.

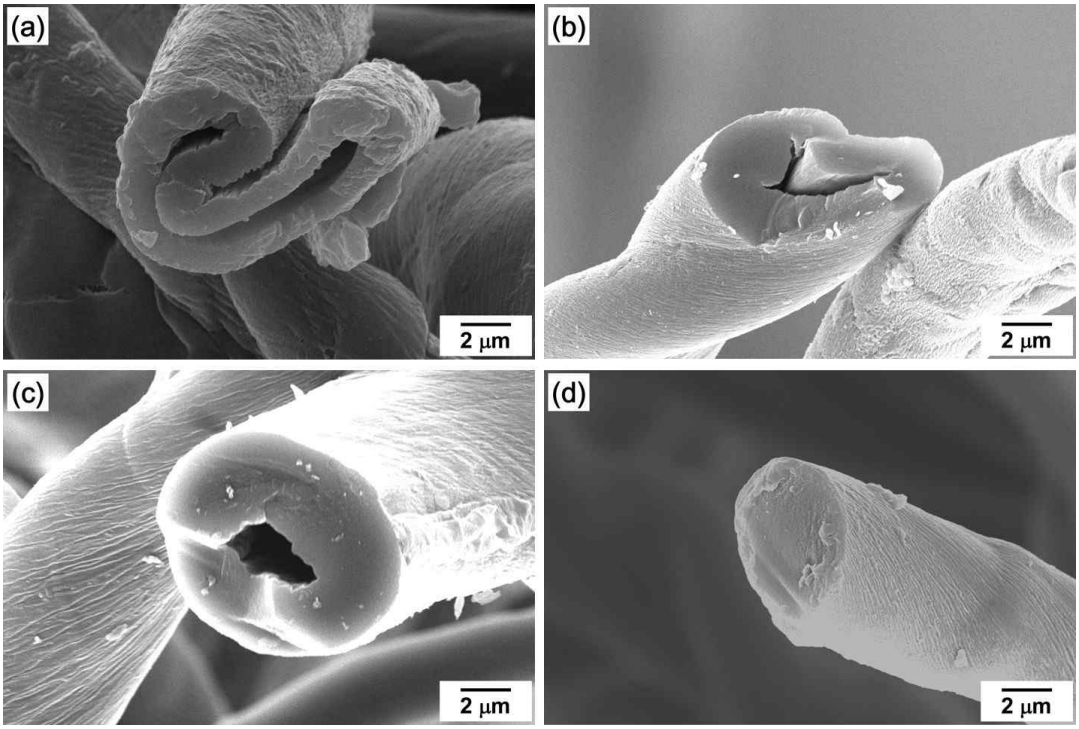

Figure 5. SEM images of the (a) C-CtF and (b-d) CM-CtF samples: (b) mercerization time of 10 min; (c) mercerization time of 40 min; and (d) mercerization time of 60 min.

Further, the C-CtF samples exhibited a helical, ribbon-like structure, which was derived from the convolutions of the non-mercerized CtF (Figure 6a). Both left- and right-handed ribbon-like structures were observed in C-CtF. In contrast, a striated, tubular structure was observed in CM-CtF(40) (Figure 6b). It is assumed that the hollow, channel-like structure was not utilized in C-CtF, because of the twisting, helical structure and the narrow lumens. However, owing to the striated, fibrillar structure and the open lumens, the hollow, channel-like structure may have developed continuously along the longitudinal direction of CM-CtF(40).

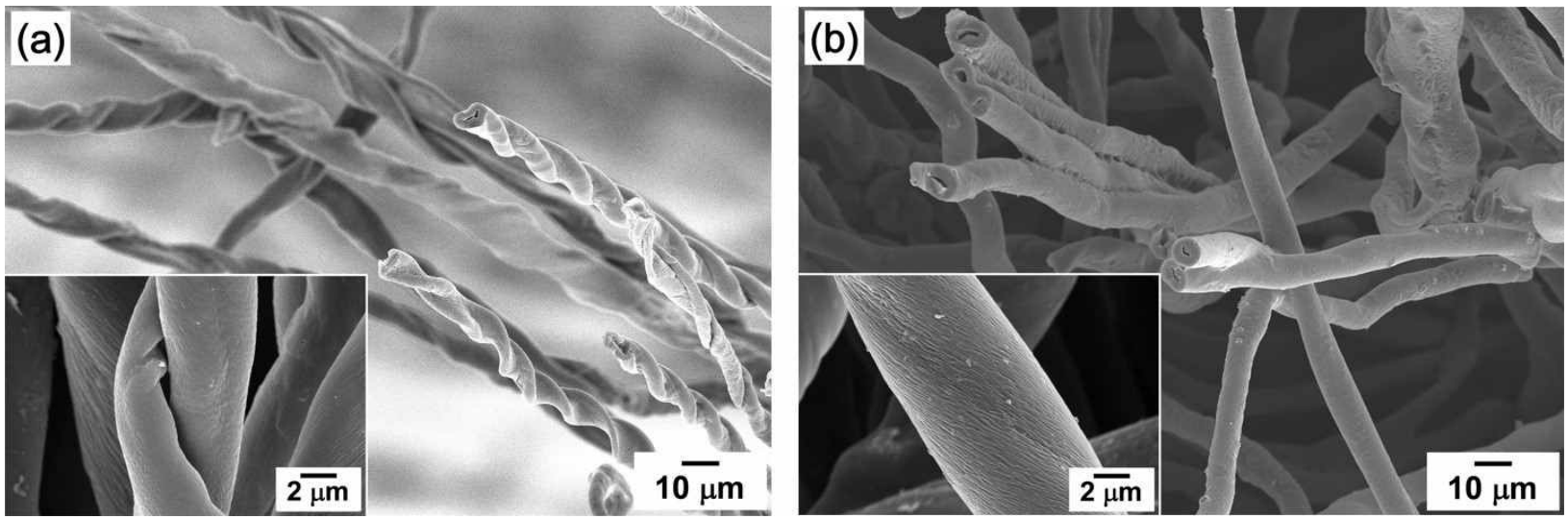

Figure 6. SEM images of (a) C-CtF and (b) CM-CtF(40). (a) A twisted, ribbon-like structure and (b) a tubular structure can be seen.

Figures 7a and b show TEM images of a microtube sectioned normal to and along the tube axis of CM-CtF(40). The images in Figure 7a and b show clearly that the hollow structure of the tube remained unchanged along its axis. Figure 7c shows high-resolution TEM image of the thin area of the tube. There exist graphitic structures with a low degree of short-range order among the amorphous structures. The inset in Figure 7c is the fast Fourier transform (FFT) of the pattern in Figure 7c. The spacings of the high-intensity broad spots, seen in the inset, range from 0.33 nm to 0.48 nm; these values are close to 0.34 nm (i.e., the (002) spacing of graphite), indicating the partial formation of graphitic structures. The FFT also shows that the graphitic structures were aligned to a certain extent. Figure 7d shows the electron energy loss (EEL) spectrum, indicating the existence of a carbon K-edge at 283 eV. It is known that the pre-edge peak of the carbon K-edge corresponds to the π-bonding state, and that the main peak of the carbon K-edge corresponds to the σ-bonding state. Thus, the appearance of the pre-edge peak indicated that there existed graphitic structures. The carbon K-edge at 283 eV in Figure 6d exhibited a noticeable pre-edge peak (red dotted circle), indicating that graphitic structures had somehow developed in the microtube. By virtue of the graphitic structures, the electrical conductivities of the carbonized CtFs prepared at 800 ℃ are about 2 S/cm.

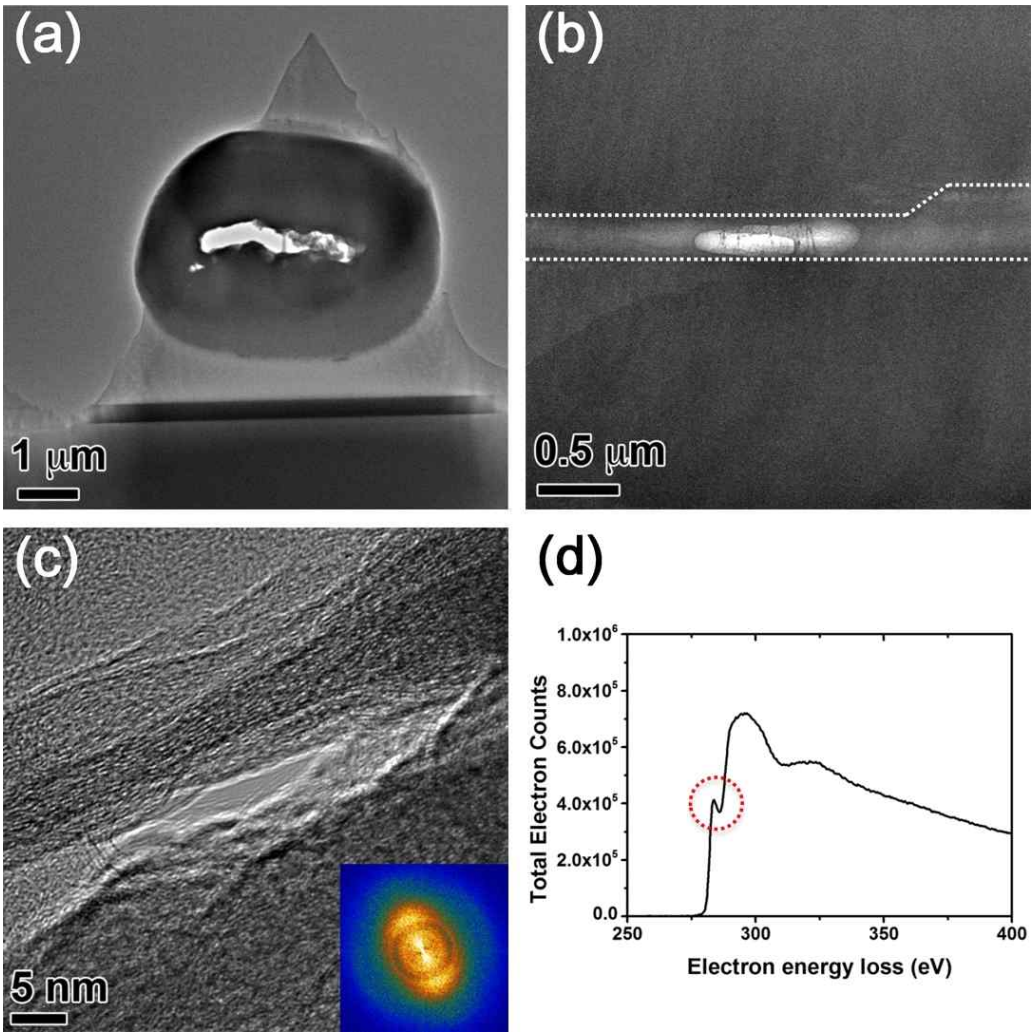

Figure 7. TEM images of cross-sections of CM-CtF(40). (a) normal to and (b) along the tube axis. The white dotted lines in (b) indicate the hollow area along the tube axis (c) High-resolution TEM image of the thin area of a microtube. The inset in (c) is the FFT of (c). (d) Background-subtracted EEL spectrum showing a carbon K-edge at 283 eV. The red dotted circle in (d) shows the pre-peak of the carbon K-edge.

N_2 adsorption analyses were performed at 77 K to determine the changes in the specific surface areas (SSAs) of the C-CtF and CM-CtF samples. The N_2 adsorption isotherms of the C-CtF and CM-CtF samples were typical type-I isotherms, exhibiting a steep N_2 uptake at lower P/P_0 values and a long plateau at higher P/P0 values, indicating uniform microporosity (Fig. 8a). Interestingly, the SSA of C-CtF, which was 203.7 m^2/g, increased gradually to 562.4 (in the case of CM-CtF(10)), and 653.75 (in the case of CM-CtF(20)) with an increase in the mercerization time, eventually reaching 726 m^2/g in the case of CM-CtF(40). In the case of CM-CtF(60), which was fully mercerized, the SSA dropped to 276.7 m^2/g; this value is close to the SSA of C-CtF. In particular, CM-CtF(40) reveals a high micropore volume of 0.26 cm^3/g along with microporous SSA of 681.7 m^2/g, whereas C-CtF prepared without mercerization time has a micropore volume of 0.07 cm^3/g along with microporous SSA of 171.0 m^2/g. It is thought that the volume of the hollow channel increased with the increase in the mercerization time because the primary and secondary walls of the fibrils swelled with the increase in the mercerization time .

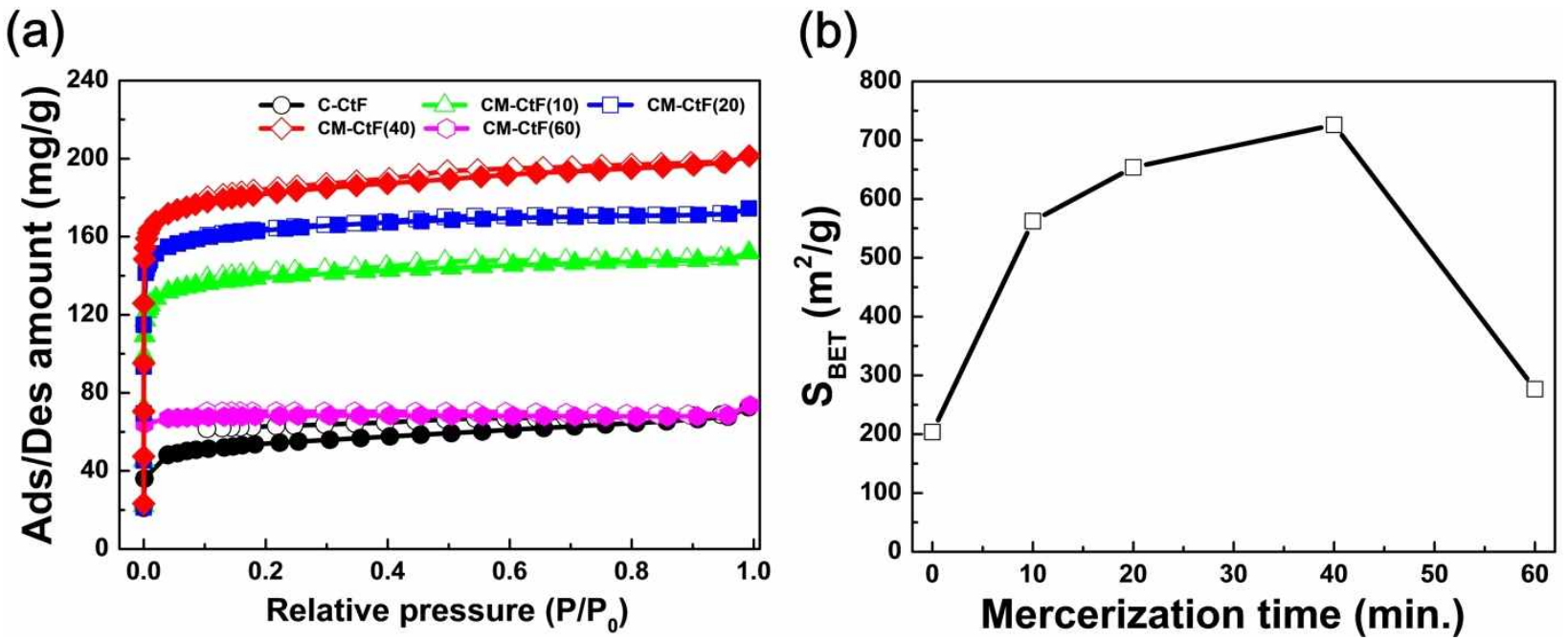

Figure 8. (a) Brunauer-Emmett-Teller (BET) isotherms of the C-CtF and CM-CtF samples. (b) Variations in the specific surface areas of the C-CtF and CM-CtF samples.

Table 1. **Pore structure parameters of C-CtF and CM-CtF samples determined by subtracting pore effect (SPE) method**

Sample	BET						
	Total SSA (m^2/g)	Micropore SSA (m^2/g)	Mesopore SSA (m^2/g)	Total pore volume (cm^3/g)	Micropore volume (cm^3/g)	Mespore volume (cm^3/g)	Mean pore width (nm)
C-CtF	203.7	171.0	32.7	0.11	0.07	0.04	0.7
CM-CtF(10)	562.4	531.7	30.7	0.23	0.20	0.03	0.6
CM-CtF(20)	653.8	621.9	31.9	0.27	0.24	0.03	0.6
CM-CtF(40)	726.7	681.7	45.0	0.31	0.26	0.05	0.6
CM-CtF(60)	276.7	274.6	2.1	0.08	0.07	0.01	0.7

5. Conclusion

I successfully fabricated carbon materials of different structures using mercerized cotton fibers. Cotton fibers have a unique hollow, channel-like structure in the middle of the fibrils. This hollow, channel-like structure tends to get squeezed, and the fibrils become twisted. However, the squeezed, hollow, and twisted structure transforms into a tube-like one after mercerization. By using the mercerized cotton fibers as carbonization precursors, I could successfully obtain different carbon materials. Most notably, carbon microtubes could be prepared from the cotton fibers subjected to mercerization for 40 min. This is contrast to twisted ribbon-like carbon, which is usually prepared from non-mercerized cotton fibers. Moreover, carbon rods lacking a hollow channel could be prepared from the fully mercerized cotton fibers. These results offer a new perspective on the fabrication of novel, structured carbon materials with various functionalities, as the method used exploits both the natural structure of cotton fibers and artificial chemical processes. Further, it was demonstrated that the specific surface area of the carbonized cotton fibers could be controlled by varying the mercerization time.

6. References

[1] J. Laine, A. Calafat, and M. Labady, *Carbon* 27, 191 **(1989).**

[2] K. Kamata, S. Suzuki, M. Ohtsuka, M. Nakagawa, T. Iyoda, and A. Yamada, *Adv. Mater.* 23, 5509 **(2011).**

[3] P. J. Wakelyn, N. R. Bertoniere, A. D. French, D. P. Thibodeaux, D. P. Triplett, M. A. Rousselle, W. R. Goynes, J. V. Edwards, L. Hunter, D. D. McAlister, and G. R. Gamble, Cotton Fiber Chemistry and Technology, CRC, New York, (**2007).**

[4] T. Okano, and A. Sarko, *J. App. Polym. Sci.* 30, 325 **(1935).**

[5] J. ordon Cook, Handbook of Textile Fibres: Natural Fibres, Woodhead, Cambridge 1984 Vol. 1.

[6] E. Jazaeri, L. Zhang, X. Wang, and T. Tsuzuki, *Cellulose* 18, 1481 **(2011).**

[7] M. Sevilla, and A. B. Fuertes, *Carbon* 47, 2281 **(2009).**

[8] Y. Liu, and H. Hu, *Fiber Polym.* 9, 735 **(2008).**

[9] D. L. Morgado, and E. Frollini, *Polímeros* 21, 111 **(2011).**

[10] Y. Yue, C. Zhou, A. D. French, G. Xia, G. Han, Q. Wang, and Q. Wu, *Cellulose* 19, 1173 **(2012).**

[11] M. M. Tang, and R. Bacon, *Pyrolysis Carbon* 2, 211 **(1964).**

Highly microporous carbon materials synthesized from fluorine-containing poly(amic acid) adsorbed in polystyrene cryogel template

1. Abstract

In this work, a highly microporous carbon material was synthesized through the combination of fluorine-containing poly(amic acid) (F-PAA), which can produce a microporous carbon material upon carbonization, and a mesoporous polystyrene (PS) cryogel. Carbonization of F-PAA at 1000 ℃ yielded a microporous carbon material with high specific surface area (SSA, ~1300 m^2/g). In addition, we prepared a PS cryogel template with microcellular structure by freeze-drying the PS solution in 1,4–dioxane. The template was then impregnated with F-PAA, followed by carbonization at 1000 ℃. Interestingly, the carbon material obtained through this approach maintained the microcellular structure of the PS cryogel template even after template pyrolysis during carbonization. Moreover, the microcellular carbon material exhibited a high SSA and a large micropore volume (~2400 m^2/g and 0.90 cm^3/g, respectively).

2. Introduction

A unique method for producing highly ordered mesoporous carbon materials, based on microcellular carbon cryogels with honeycomb structure fabricated via uniaxial freeze-drying, has been proposed recently [1,2]. Since the solvents suitable for this approach are limited to water or 1,4–dioxane, only polymers soluble in these solvents, such as polyvinyl alcohol,3 polystyrene (PS) [4,5], polyurethane [6], and polylactide [7], were used to prepare polymer cryogels by freeze-drying. However, these polymers are not useful as carbonization precursors due to their low carbonization yield, and their microcellular morphology is not maintained after heat treatment. For this reason, only a few studies have involved the use of polymer cryogels to produce highly ordered carbon materials by freeze-drying [1,2,8]. Alternative approaches to prepare porous carbon materials by adsorbing additional carbon sources into a freeze-dried porous polymer cryogel template have been investigated [9,10]. However, the porous carbon materials obtained from the polymer cryogel template were mesoporous and possessed a specific surface area (SSA) of ca. 800 m^2/g, which is too low for the application of these materials as charge storage materials for electric double-layer capacitors (EDLC) [11].

Polyimides (PIs), synthesized by the thermal imidization of poly(amic acid) (PAA) precursors, have been considered as carbonization precursors because of their ability to retain the structural morphology even after carbonization, due to their homogeneous shrinkage, high carbonization yields, and absence of crack formation during carbonization [8,12]. This is a unique case where the molecular structure of the polymer precursors and the structural morphology of the polymer films control the structural morphology of the resulting carbon films. For these reasons, PIs have been used as carbonization precursors for the synthesis of highly oriented graphite films [13], macroporous carbon materials [14], and thin carbon membranes [15].

Recently, Inagaki et al. reported that PIs containing fluorine moieties exhibited a significantly enhanced microporous surface area when the fluorine content was increased [16]. The microporous surface area of PIs containing $–CF_3$ groups showed a strong dependence on the number of these groups in each PI repeating unit; moreover, the fluorine-containing PIs maintained the structure of the precursor after carbonization and possessed a high microporous surface area of 1400 m^2/g.

The combination of fluorine-containing PAA (F-PAA) with the polymer cryogel template appears potentially interesting, because it could enable the production of carbon materials with high SSA by incorporating the high microporous surface area and microporous structure of the F-PAA within the microcellular and mesoporous structure of the polymer cryogel template. In this work, I prepared microcellular carbon materials by adsorption of the F-PAA solution into a microcellular PS cryogel template synthesized by the uniaxial freeze-drying method. PS was selected as base material for the polymeric cryogel template because, whereas its low melting point and carbonization yield limit its use as a precursor for carbonization, it represents a suitable source material for the microcellular cryogel template.

3. Experiment

3.1 Materials

All experiments were performed in argon atmosphere. Polystyrene (PS, Mw = 280000)was purchased from Sigma-Aldrich Co.(USA).N–Methyl–2–pyrrolidone (NMP) was distilled prior to use. Other chemical compounds such as 4,4′–(hexafluoroisopropylidene)diphthalic anhydride (6FDA) and 3,3′–dihydroxybenzidine (HAB) were purchased from commercially available sources.

3.2 Synthesis of F-PAA

The molecular structure of a repeating unit of F-PAA synthesized from 6FDA and HAB is shown in Scheme 3.1. First, HAB (0.49 g, 2.5 mmol) was dissolved in NMP (6 mL) and stirred at room temperature. 6FDA (1.0 g, 2.5 mmol) was then added dropwise to the solution at the same temperature. The mixture was stirred at the same temperature for 24 h and quenched with H_2O. The resulting precipitate was collected by filtration and dried in a vacuum oven at 60 ℃ for 24 h. The as-synthesized F-PAA showed good solubility in ethanol.

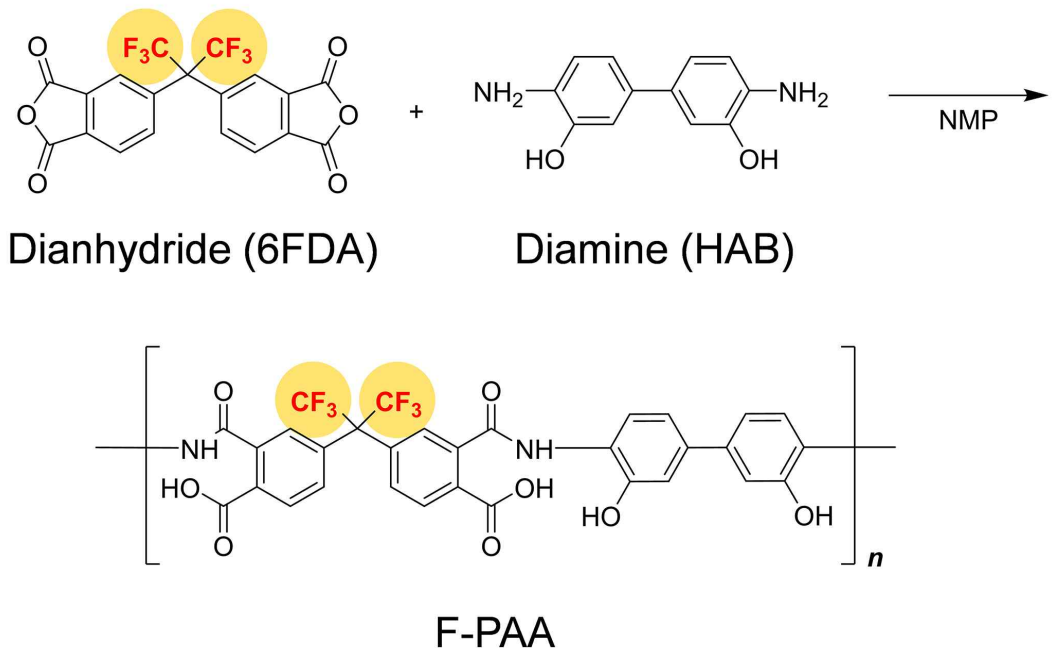

Scheme 1. Schematic molecular structure of F-PAA.

3.3 Preparation of PS cryogel template

PS cryogel template was synthesized by uniaxial freeze-drying method, as shown in Scheme 2. PS solution was prepared by dissolving PS (5.0 wt%) into 1,4–dioxane, and transfered to a polypropylene (PP) test tube with 1.2 mm thickness, 100 mm length, and 10 mm diameter. Then the PS solution was uniaxially frozen by dipping the test tube into a liquid nitrogen bath with a constant rate of 10 cm/h. After dipping the PS solution was complete, the frozen PS solution was freeze-dried at -5 ℃ for 3 days.

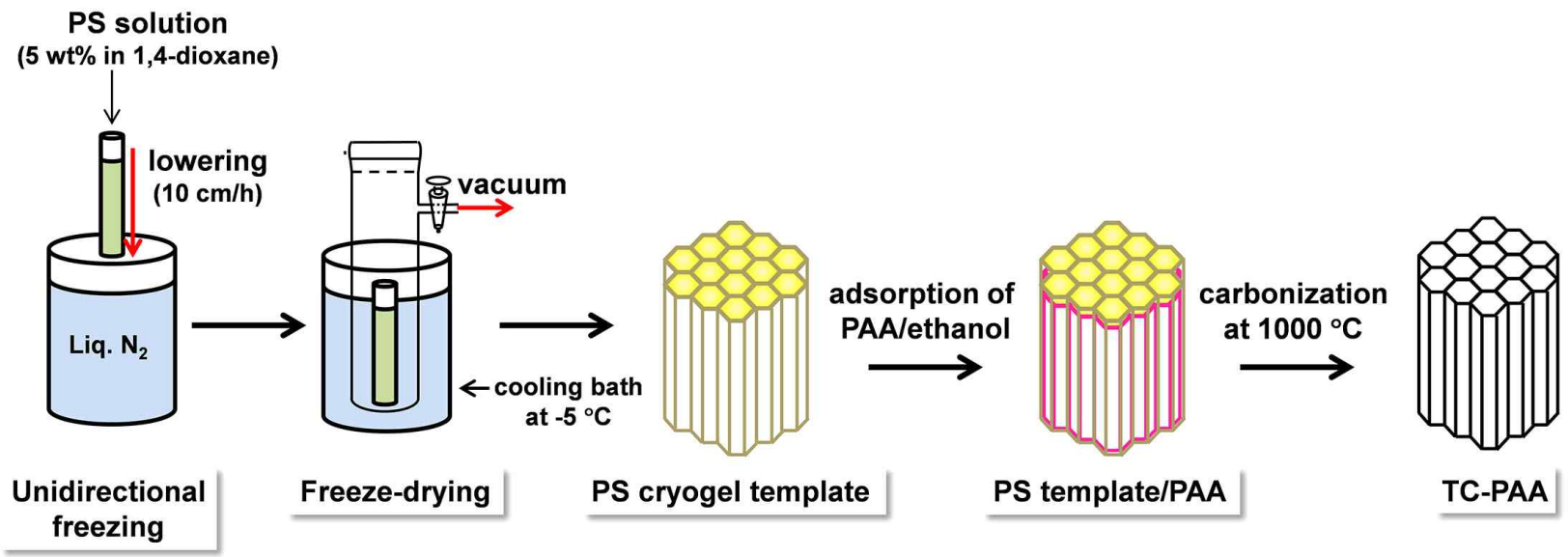

Scheme 2. Schematic illustration for preparation of PS cryogel template and TC-PAA with microcellular morphology.

3.4 Preparation of microcellular carbon cryogel

The PS template/PAA complex was prepared by adsorption of a F-PAA ethanol solution (15 wt%) into the freeze-dried PS cryogel template at room temperature for 5 min. After the adsorption, the PS template/PAA complex was dried in a vacuum oven for 2 h at room temperature. These two processes were repeated 3 times. Then, in order to remove the PS cryogel template, the PS template/PAA complex was carbonized at 1000 ℃ under argon gas flow at a heating rate of 10 ℃/min. The carbonized PS template/PAA complex will hereafter be abbreviated as TC-PAA. A reference RC-PAA sample was also prepared with a carbonized material from F-PAA, *i.e.*, without using the PS template.

3.5 Characterization

The structural morphologies of the obtained samples were observed by field-emission scanning electron microscope (FE-SEM, Nova Nano SEM 450, FEI Co., USA). For the SEM analysis, the samples were frozen by liquid nitrogen to prevent transformation, and cut with straight razor in both vertical and horizontal directions. The thermogravimetric differential thermal analysis (TG-DTA, TA instrument, USA) of PS cryogel template, F-PAA and PS template/PAA samples were obtained under nitrogen gas flow at a heating rate of 10 ℃/min. Specific surface areas (SSAs) of carbonized F-PAA and carbonized PS template/PAA samples were measured by nitrogen gas adsorption technique (BELSORP-max, BEL Japan, Inc., Japan). Samples were also analyzed by Fourier-transform infrared spectroscopy (FT-IR, Nicolet iS 10, Thermo Scientific, USA). The electrical conductivity of TC-PAA was measured by a 4-point probe method (FPP-RS8, DasolEng, Korea).

4. Results and Discussion

TG-DTA of PS cryogel template, F-PAA and PS template/PAA were measured from 0 to 950 ℃ under nitrogen gas flow at a heating rate of 10 ℃/min (Figure 1). According to the TG-DTA results, the degradation temperature of PS cryogel template were 400 ℃ and weight-loss percent was 99%. Weight-loss of F-PAA occurred in two stages, and the first stage in 150–250 ℃ was assigned to the imidization of the F-PAA precursor. The second stage in 400–500 ℃ was attributed to the thermal conversion of PI to polybenzoxazole owing to cyclodecarboxylation ($-CO_2$). In the TG-DTA curve of PS template/PAA, the weight-loss peaks of PS and PAA existed, and three sequence degradation peaks were observed in the temperature range of 350–700 ℃. These peaks were mainly due to a breakage of carbonyl groups in the imide moiety. From the char yield of A result, the mass fraction of PS template/PAA was estimated to be ca. 80 wt% (at 300 ℃) of total mass, and the mass fraction of F-PAA in the PS template/PAA was estimated to be 52 wt% (at 480 ℃). After thermal decomposition above 900 ℃, less than 32 wt% of initial weight was observed in the A curve of the PS template/PAA complex.

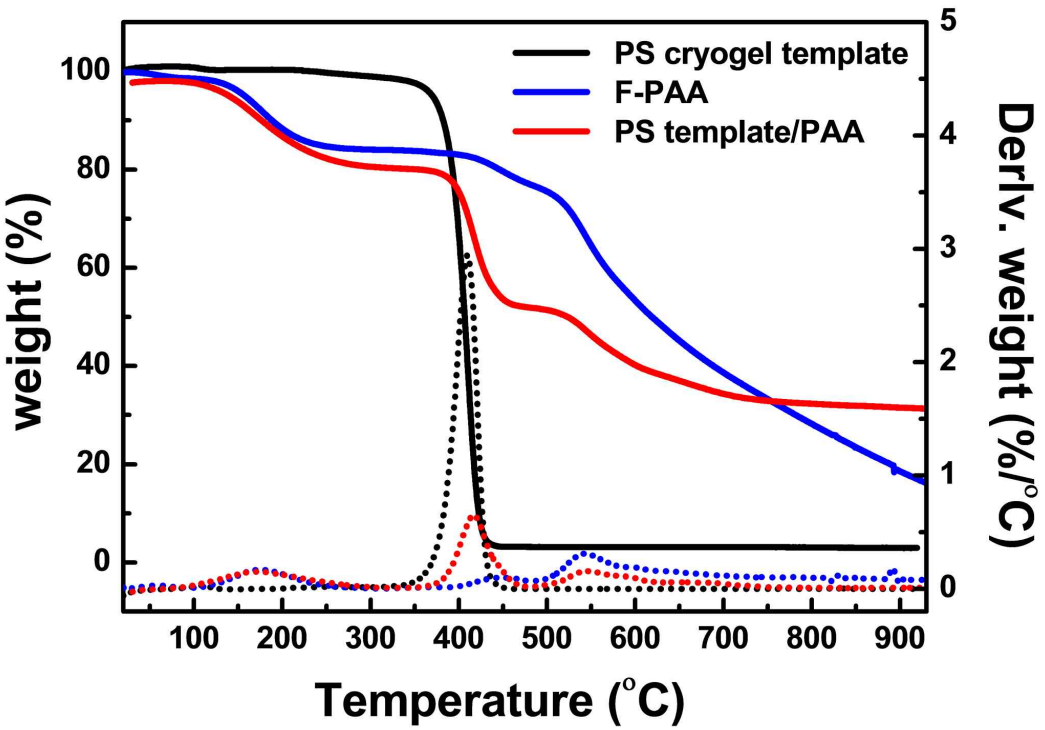

Figure 1. TG-DTA curves of the PS cryogel template, F-PAA and PS template/PAA.

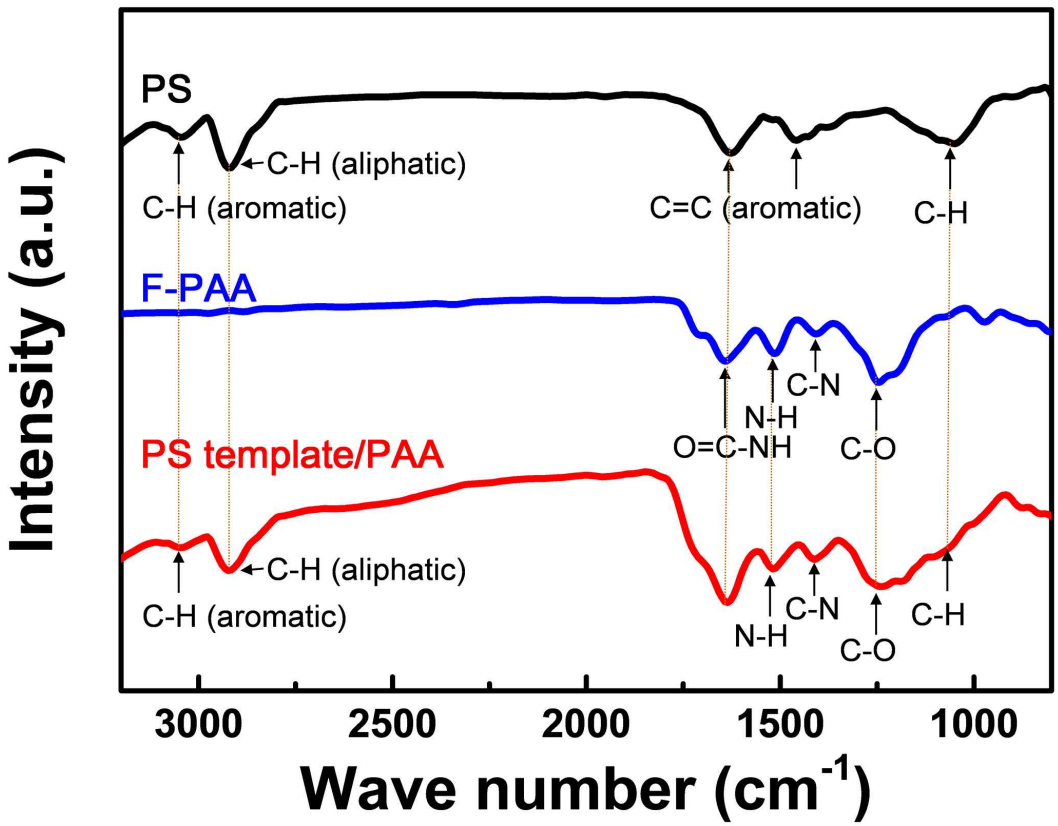

Figure 2. FT-IR spectra of PS cryogel template (black line), F-PAA (blue line) and PS template/PAA (red line).

Figure 2 show the FT-IR spectra measured for the PS cryogel template, F-PAA, and PS template/PAA complex. The FT-IR spectra of PS cryogel template revealed characteristic peaks at 3040 cm^{-1} (ν_{C-H}, aromatic), 2918 cm^{-1} ($\nu_{as,C-H}$, aliphatic), 1620 cm^{-1} ($\nu_{C=C}$, aromatic), 1457 cm^{-1} ($\nu_{C=C}$, aromatic), and 1070 cm^{-1}(ν_{C-H}, aromatic). In the case of F-PAA, the characteristic peaks at 1645 cm^{-1} ($\nu_{O=C-NH}$, amide), 1520 cm^{-1}(ν_{N-H}, amide), 1410 cm^{-1}(ν_{C-N}, amide), and 1255 cm^{-1}(ν_{C-O}, phenol) were observed. The FT-IR spectra of the PS template/PAA complex exhibited peaks characteristic of both the PS cryogel template and F-PAA. For example, absorption peaks corresponding to the methylene vibration in PS and the amide group of PAA were observed, indicating that the PS template and PAA were successfully adsorbed into the PS cryogel template.

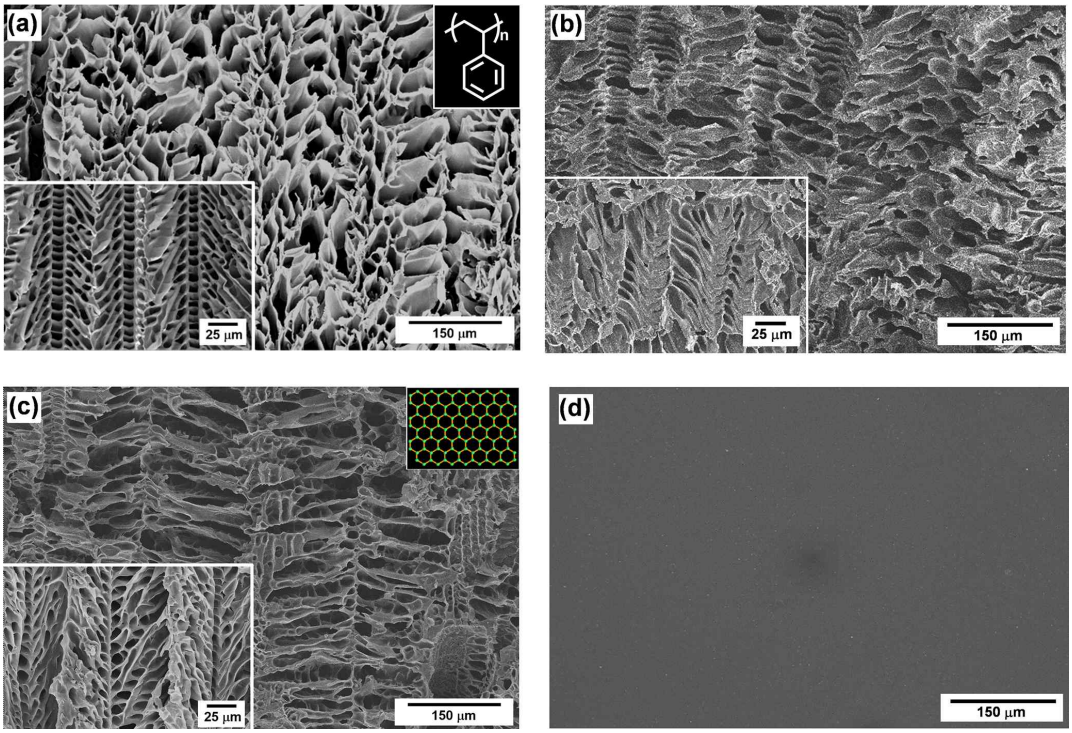

Figure 3. SEM images of (a) PS cryogel template, (b) PS template/PAA, (c) TC-PAA, and (d) RC-PAA. Insets are the photographs of vertical cross section of PS cryogel template, PS template/PAA and TC-PAA, respectively.

Following carbonization of the PS template/PAA complex at 1000 ℃. TC-PAA was obtained as a black solid with a carbonization yield of ca. 18 wt%. The structural morphology of PS cryogel template, PS template/PAA, TC-PAA, and RC-PAA was investigated by FE-SEM, and the images are shown in Figure 3. Figure 3a highlights the unique microcellular structure of the PS cryogel template prepared by uniaxial freeze-drying. This microcellular structure was successfully introduced into the PAA solution adsorbed in the PS cryogel template, as shown in Figure 3b. The microcellular morphology was also observed in the vertical section of TC-PAA in Figure 3c, indicating that the structure of the PS template/PAA complex was maintained after the PS template was removed by carbonization. On the other hand, Figure 3d shows that RC-PAA does not exhibit an ordered structure. TC-PAA exhibited a honeycomb structure in the horizontal section, different from the vertical section. This feature is quite different from the PS cryogel template which is characterized by bamboo-like channels connected along the width direction. The average diameter of the PS cryogel template was ca. 12.4 ㎛, and the average pore width of TC-PAA was ca. 11.3 ㎛, which is smaller than the corresponding length (25.0 ㎛). This feature was probably due to the collapse of the weak wall during carbonization.

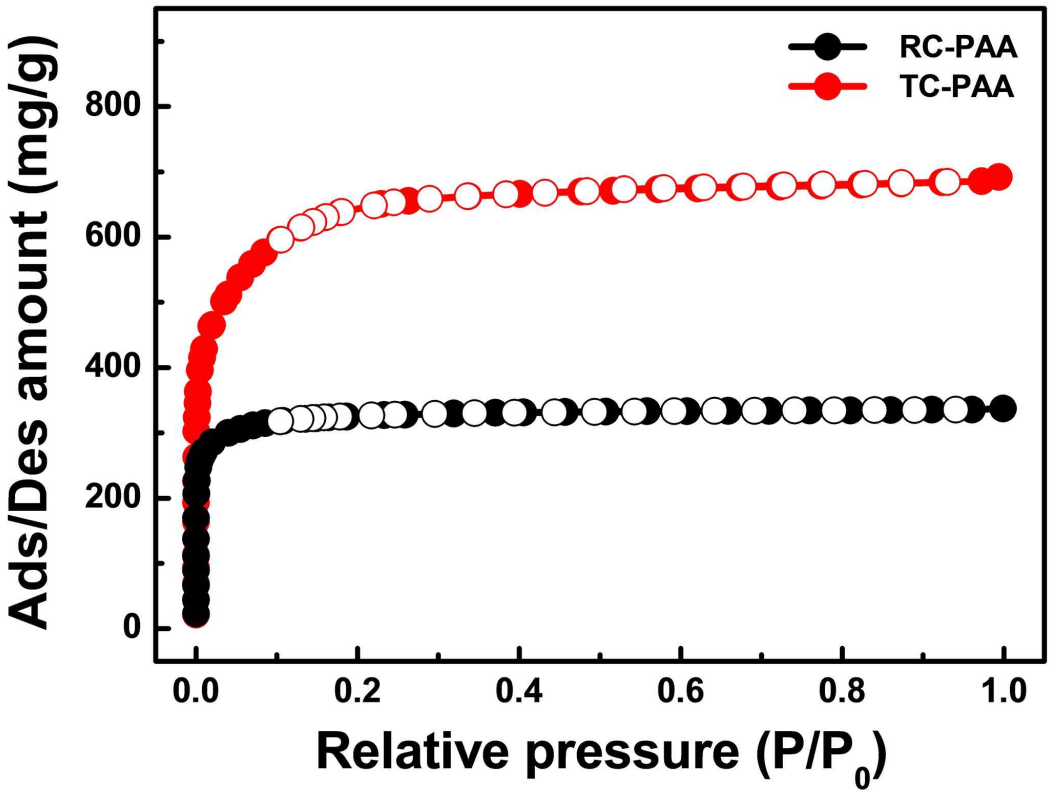

Figure 4. Nitrogen gas adsorption isotherms of RC-PAA and TC-PAA at 77 K.

***Table 1*. Pore structure parameters of carbon material samples.**

Sample	Total SSA (m^2/g)	Mesopore SSA (m^2/g)	Micropore SSA (m^2/g)	Total pore volume (cm^3/g)	Mesopore volume (cm^3/g)	Micropore volume (cm^3/g)	Mean pore width (nm)
RC-PAA	1277	18	1259	0.52	0.02	0.50	0.6
TC-PAA	2443	227	2216	1.07	0.17	0.90	0.8

N_2 adsorption and desorption isotherms were measured at 77 K, in order to determine the SSAs of RC-PAA and TC-PAA. The results are shown in Figure 4 and Table 1. The N_2 adsorption isotherms in Figure 4 show a typical type I behavior, according to the IUPAC classification. RC-PAA and TC-PAA exhibited SSAs of 1277 m^2/g and 2443 m^2/g, respectively. In particular, the micropore SSA and volume of TC-PAA were 2216 m^2/g and 0.90 cm^3/g, respectively, whereas the micropore SSA and volume of RC-PAA were 1259 m^2/g and 0.5 cm^3/g, respectively. Generally, microporous (< 2 nm) and mesoporous (2–50 nm) surface areas depend on the content of pendant groups and on the structural morphology. The good surface properties of TC-PAA were ascribed to the following features: (i) the microcellular structure of the PS cryogel template, which derived from the uniaxial freezing of the PS solution. The concentration of the solvent decreased upon its crystallization during the uniaxial freezing, inducing phase separation between solvent and polymer. Due to the phase separation, the PS was excluded from the solvent crystals, and formed a honeycomb structure along the direction of solvent freezing [17]; (ii) the microcellular structure of F-PAA, which originated from and maintained the microcellular structure of the PS cryogel template. After adsorption of the F-PAA ethanol solution, the PS template would have honeycomb porous channels filled with the dense F-PAA. As shown by the SEM images in Figure 3, the PS cryogel template disappeared after carbonization, but F-PAA was converted to TC-PAA, retaining the microcellular structure of the PS cryogel; (iii) the connected bamboo-like channels, which originated from carbonization of the F-PAA. These channels had an open structure, which enabled gases to easily permeate them and be absorbed; (iv) the large amount of micropores, which originated from carbonization of F-PAA [15]. The synthesis of F-PAA from dianhydride and diamine is illustrated in Scheme 1. The synthesized F-PAA had -CF3 and -OH pendant groups in the polymer backbone, from which they started to be eliminated at around 450 ℃ and 600 ℃, respectively. The elimination of

these pendant groups helped to form a highly microporous microcellular carbon material, and also led to an increase in the SSA of the material. Based on these considerations, we conclude that TC-PAA showed enhanced mesoporous properties due to features (i)-(iii), and microporous properties due to (iv).

As the high SSA of TC-PAA appeared suitable for applications to EDLCs, we evaluated its electrical properties by measuring the electrical conductivity. In order to measure the electrical conductivity of the sample, porous TC-PAA paper was prepared by filtrating a solution of TC-PAA powder in distilled H_2O. The paper was then contacted in the van der Pauw configuration by four Au wires using Ag paste. The measured electrical conductivity of TC-PAA was around 5.7×10^{-3} S/cm, a value comparable to other porous carbon materials for EDLC applications, taking into account that the sample was prepared as powder-type, which is different from the pellet-type reference samples [18]. These results indicate that the SSA value and electrical conductivity of TC-PAA can enable it become a potential charge storage material for EDLC applications.

5. Conclusion

A polystyrene cryogel template was prepared from a PS solution in 1,4-dioxane. The good solubility of PS in 1,4-dioxane enabled the uniaxial freeze-drying approach to be applied. A PS template/PAA complex with honeycomb structural morphology was obtained by adsorbing an ethanol solution of poly(amic acid) containing fluorine moieties into the PS cryogel template. Because of the high carbonization yield and homogeneous adsorption of F-PAA, a microcellular TC-PAA carbon material, which retained the honeycomb structural morphology, was successfully fabricated by carbonization of the PS template/PAA complex. The TC-PAA material showed a specific surface area of ~2400 m^2/g and a micropore volume of 0.90 cm^3/g, which are higher than those of F-PAA carbonized without the PS template.

The method presented in this work appears suitable to produce hierarchical carbon materials with modular pore structures from a variety of polymeric precursors. As a matter of fact, modular micro- and mesopore structures can be successfully prepared from the fluorine-containing poly(amic acid) adsorbed in the polystyrene cryogel template. These modular pore structures are rather difficult to produce from conventional activated carbon materials, which have a random pore size distribution and irregular pore structures. Therefore, we envisage that the present method will be advantageous because it can be used to fabricate highly porous carbon materials with a regular pore size distribution, utilizing various polymer precursors, and it has the potential to provide high-performance carbon materials with regular hierarchical pore structures. Moreover, the porous carbon materials prepared by this method are expected to be effective charge storage materials for EDLC applications.

6. References

[1] S. A. Al-Muhtaseb, J. A. Ritter, *Adv. Mater.* 15, 101 **(2003)**.

[2] H. Nishihara, S. R. Mukai, H. Tamon, *Carbon* 42, 899 **(2004).**

[3]H. F. Zhang, I. Hussain, M. Brust, M. F. Butler, S. P. Rannard, A. I. Cooper, *Nat. Mater.* 4, 787 **(2005)**.

[4] J. H. Aubert, R. L. Clough, *Polymer* 26, 2047 **(1985)**.

[5] G. Widawski, M. Rawiso, B. Francois, *Nature* 369, 387 **(1994)**.

[6] J. H. de Groot, A. J. Nijenhuis, P. Bruin, A. J. Pennings, R. P. H Veth, J. Klompmaker, H. W. B Jansen, *Colloid. Polym. Sci.* 268, 1073 **(1990)**.

[7] C. Schugens, V. Maquet, C. Grandfils, R. Jerome, P. Teyssie, *Polymer* 37, 1027 **(1996)**.

[8] Y. Choi, K. P. Singh, J. D. Park, N. You, C. Yang, M. Goh, J. Yu, *Energy Technol.* in press **(2015)**, doi: http://dx.doi.org/10.1002/ente.201500225.

[9] M. Barrow, A. Eltmimi, A. Ahmed, P. Myers, H. F. Zhang, *J. Mater. Chem.* 22, 11615 **(2012).**

[10] Y. B. Hong, H. Yeo, Y. Choi, N. You, S. H. Lee, M. Goh, *Synth. Met.* 196, 33 **(2014).**

[11] L. Wei, G. Yushin, *Nano Energy* 1, 552 **(2012)**

[12] M. Inagaki, M. Sato, T. Takeichi, A. Yoshida, Y. Hishiyama, *Carbon* 30, 903 **(1992)**.

[13] C. Bourgerette, A. Oberlin, M. Inagaki, *J. Mater. Res.* 10, 1024 **(1995)**.

[14] M. Inagaki, T. Morishita, A. Kuno, T. Kito, M. Hirano, T. Suwa, K. Kusakawa, *Carbon* 42, 497 **(2004)**.

[15] N. Ohta, Y. Nishi, T. Morishita, T. Tojo, M. Inagaki, *Carbon* 46, 1350 **(2008)**.

[16] N. Ohta, Y. Nishi, T. Morishita, T. Tojo, M. Inagaki, *TANSO* 233, 174 **(2008)**.

[17] J. Kim, K. Taki, S. Nagamine, M. Ohshima, *Langmuir* 25, 5304 **(2009)**.

[18] M. J. Bleda-Martínez, J. A. Maciá-Agulló, D. Lozano-Castelló, E. Morallón, D. Cazorla-Amorós, A. Linares-Solano, *Carbon* 43, 2677 **(2005)**.

List of pubication

publication

Jin Won Yu, Yong-Mun Choi, Seung Min Kim, Jae-Kwan Lee, Nam-Ho You, Munju Goh
"Synthesis of Twisted Ribbon-like Carbon, Carbon Microtubes and Carbon Rod from Mercerized Cotton Fiber"
Synthetic Metals. 2014, **206**, 115-119.

Jin Won Yu, Yong-Mun Choi, Jin Jung, Nam-Ho You, Dong Su Lee, Jae Kwan Lee, Munju Goh
"Highly Microporous Carbon Materials Synthesized from Fluorine-Containing Poly(amic acid) Adsorbed in Polystyrene Cryogel Template"
Synthetic Metals. 2015, *accept.*

Jin Won Yu, Jin Jung, Yong-Mun Choi, Jae Hun Choi, Jaesang Yu, Jae Kwan Lee, Nam-Ho You, Munju Goh
“Enhancement of Crosslink Density, Glass Transition Temperature, and Strength of Epoxy Resin by using Functionalized Graphene Oxide Co-curing Agents”
Polymer chemistry. 2015, *in press (selected as cover).*

Poster

1. Jin Won Yu, Yong-Mun Choi, Seung Min Kim, Hyeonuk Yeo, Jae-Kwan Lee, Nam-Ho You, Munju Goh,

“Carbon Micro-tubes Prepared from Mercerized Cotton Fibers”

탄소학회 추계 학술대회. 2014

Carbon Micro-tubes Prepared from Mercerized Cotton Fibers

Jin Won Yu[1,2], Yong-Mun Choi[1], Seung Min Kim[1], Hyeonuk Yeo[1], Jae-Kwan Lee[2], Nam-Ho You[1], Munju Goh[1,*]

[1]Carbon Convergence Materials Research Center, Korea Institute of Science and Technology (KIST), Chudong-ro 92, Bongdong-eup, Wanju-gun, Jeollabuk-do, 565-905, Korea
[2]Department of Carbon Materials, Chosun University, Gwangju, 561-756, Republic of Korea
E-mail: goh@kist.re.kr

Introduction

❖ Cellulose with unique nanostructures

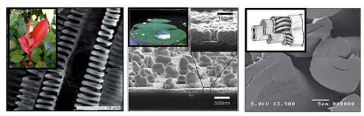

Red robin | Rotus leaf | Cotton fiber

❖ Carbonization of mercerized cotton fiber

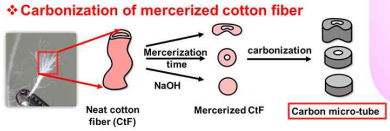

❖ **Synthesis of morphologically controlled carbon materials from mercerized cotton fiber**

1. Morphology control of CtF by varying mercerization time
2. Morphology-retaining carbonization of CtF
3. Estimate the surface area of carbonized CtF

Experiment

Mercerization with NaOH solution (15 wt%)
↓
Wash with (HCl and DI-water)
↓
Drying at room temperature
↓
Carbonization (at 800 °C for 1 h, 10 °C/min)

Result and discussions

➢SEM image

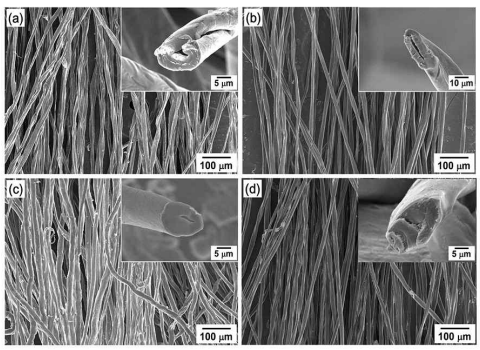

Fig. 1. SEM images of CtF (a) and M-CtFs (b-d). b) Mercerization time of 10 min. c) Mercerization time of 40 min. d) Mercerization time of 60 min.

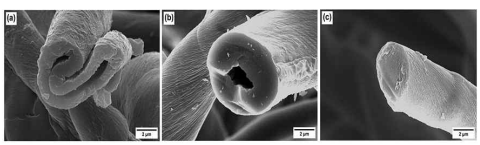

Fig. 2 SEM images of C-CtF (a) and CM-CtFs (b-c). b) Mercerization time of 40 min. c) Mercerization time of 60 min.

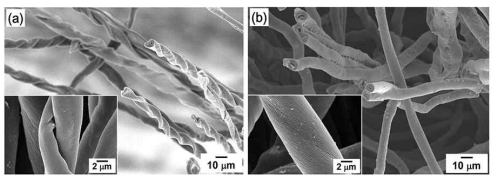

Fig. 3 SEM images of (a) C-CtF and (b) CM-CtF (40). (a) Twisted ribbon-like structure and (b) tubular structures are observed.

➢TEM image

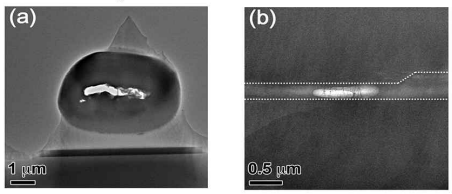

Fig. 4 TEM images of cross-sectioned areas (a) normal to and (b) along a tube axis.

➢BET

	C-CtF	CM-CtF (10)	CM-CtF (20)	CM-CtF (40)	CM-CtF (60)
SSA (m^2/g)	203.7	562.4	653.8	726	276.7

* specific surface area (SSA)

Summary

❖Various carbon micro-tubes (twisted, ribbon and round-tubular shape) were successfully prepared by carbonizing the mercerized cotton fibers.

❖After mercerization, the specific surface area (SSA) of cotton fibers were increased from 203.7 m^2/g to 726 m^2/g.

Korea Institute of Science and Technology Institute of Advanced Composite Materials

2. Jin Won Yu, Jin Jung, Yong-Mun Choi, Nam-Ho You, Munju Goh "Highly Microporous Carbon Materials Synthesized Using Poly(amic acid) Containing Fluorine Adsorbed in Polystyrene Cryogel Template" 한국고분자학회 추계 학술대회. 2015

Highly Microporous Carbon Materials Synthesized Using Poly(amic acid) Containing Fluorine Adsorbed in Polystyrene Cryogel Template

Jin Won Yu, Jin Jung, Yong-Mun Choi, Nam-Ho You, Munju Goh,*

Carbon Convergence Materials Research Center, Korea Institute of Science and Technology (KIST),
Chudong-ro 92, Bongdong-eup, Wanju-gun, Jeollabuk-do, 55324, Korea
E-mail: goh@kist.re.kr

Introduction

❖ **Cryogel**

➢ **materials**

- Polystyrene, polyurethane, polylactide, polyvinyl alcohol etc

➢ **Cryogel**

- Honeycomb structure
- Microcellular Morphologies
- **Low microporosity and SSA**

➢ **Polyamic acid containing fluorine(PAA)**

- High microporosity and high SSA*
- High carbonization yield
- Structure was maintain after carbonized

* SSA = specific surface area

❖ **This work**

✓ **Synthesis of microcellular PS *via* unidirectional freeze-drying method.**

✓ **Absorption of PAA solution using microcellular PS as a template.**

Highly microporous carbon materials

Experimental

❖ **Polystyrene** ❖ **Polyamic acid & polyimide**

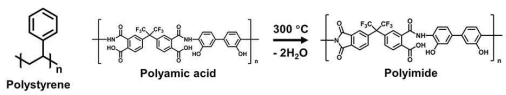

❖ **Preparation of PS cryogel template and honeycomb structured carbon materials**

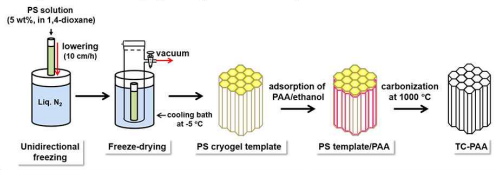

Results & Discussion

TG-DTA

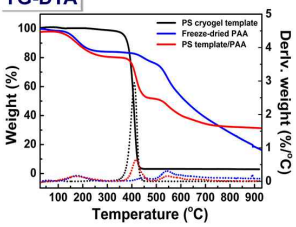

Figure 1. TG and DTA curves of the PS cryogel template, freeze-dried PAA and PS template/PAA.

SEM

* TC-PAA = PS template/PAA after carbonized

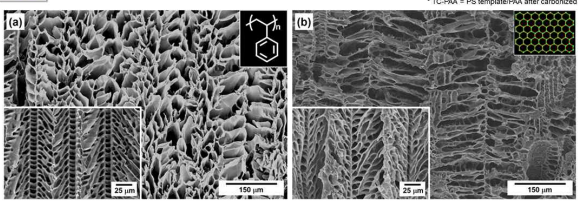

Figure 3. SEM image of (a) PS cryogel template and (b) TC-PAA*. Insets are the photographs of vertical cross section of PS cryogel template and TC-PAA, respectively.

FT-IR

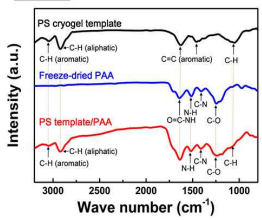

Figure 2. FT-IR spectra of (black line) PS cryogel template, (blue line) PAA and (red line) PS template/PAA.

BET

* RC-PAA = freeze-dried PAA after carbonized

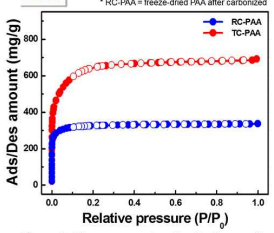

Figure 4. Nitrogen gas adsorption isotherms of RC-PAA* and TC-PAA at 77 K.

Total specific surface area

- **RC-PAA = 1200 m^2/g**
- **TC-PAA = 2400 m^2/g**

Porous volume table

Sample	Mesopore SSA (m^2/g)	Micropore SSA (m^2/g)	Total pore Volume (cm^3/g)	Mesopore volume (cm^3/g)	Micropore volume (cm^3/g)	Mean pore Width (nm)
RC-PAA	20	1300	0.52	0.02	0.50	0.6
TC-PAA	230	2200	1.07	0.17	0.90	0.8

Summary

✓ PS cryogel template/poly(amic acid) (PAA) was prepared by absorption of PAA into the PS template.

✓ Microcellular meso & microporous carbon material was prepared by carbonization of PS template/PAA.

✓ Carbon material from PS template/PAA showed SSA of **2400 m^2/g** and micropore volume of **0.90 cm^3/g**.

Korea Institute of Science and Technology Institute of Advanced Composite Materials

Acknowledgment

The studies presented in this master's thesis have been carried out under the direction of Professor Jae Kwan Lee at Department of Carbon Materials, Chosun University, and Dr. Munju Goh at Institute of Advanced Composite Materials, Korea of Science and Technology from 2014 to 2015. The studies concerned with the development of high-performance epoxy nanocomposite using functionalized graphene oxide.

The author is also appreciating to Dr. Bon-Cheol Ku and Dr. Nam Ho You for their valuable suggestions and discussions. The authors would like to thank to Mr. Yong-Mun Choi, Mr. Jin Jung, Mr. Jae Hun Choi, Mr. Hyeonuk Yeo, Ms. Hyeonju Kim, Ms. Han-Seok Chae, Ms. Hwa Jung Kim, Mr. Hanbin Jeong, Mr. Kyoung kuk Koh.

Finally, the author expresses her deep appreciation to her familys, Madame Jungiim Eom and Mr Hyeon seok Jeong for their constant assistance and encouragement.

2015년 10월

Yu Jin Won